Alexander A. Kokhanovsky and Gerrit de Leeuw
(Editors)

Satellite Aerosol Remote Sensing over Land

Springer

Published in association with
Praxis Publishing
Chichester, UK

PRAXIS

Editors
Dr Alexander A. Kokhanovsky
Institute of Environmental Physics
University of Bremen
Germany

Professor Gerrit de Leeuw
Finnish Meteorological Institute & University of Helsinki, Finland
TNO, Utrecht, The Netherlands

SPRINGER–PRAXIS BOOKS IN ENVIRONMENTAL SCIENCES
SUBJECT *ADVISORY EDITOR*: John Mason M.B.E., B.Sc., M.Sc., Ph.D.
EDITORIAL *ADVISORY BOARD MEMBER*: Dr Alexander A. Kokhanovsky, Ph.D. Institute of Environmental Physics, University of Bremen, Bremen, Germany

ISBN 978-3-540-69396-3 Springer Berlin Heidelberg New York

Springer is part of Springer-Science + Business Media (springer.com)

Library of Congress Control Number: 2008943659

Apart from any fair dealing for the purposes of research or private study, or criticism or review, as permitted under the Copyright, Designs and Patents Act 1988, this publication may only be reproduced, stored or transmitted, in any form or by any means, with the prior permission in writing of the publishers, or in the case of reprographic reproduction in accordance with the terms of licences issued by the Copyright Licensing Agency. Enquiries concerning reproduction outside those terms should be sent to the publishers.

© Praxis Publishing Ltd, Chichester, UK, 2009

The use of general descriptive names, registered names, trademarks, etc. in this publication does not imply, even in the absence of a specific statement, that such names are exempt from the relevant protective laws and regulations and therefore free for general use.

Cover design: Jim Wilkie
Project copy editor: Mike Shardlow
Author-generated LaTex, processed by EDV-Beratung, Germany

Printed in Germany on acid-free paper

10 Polarimetric remote sensing of aerosols over land surfaces

Brian Cairns, Fabien Waquet, Kirk Knobelspiesse, Jacek Chowdhary, Jean-Luc Deuzé

1. Introduction

Writing from the *S.S. Narkunda*, near Aden, C. V Raman noted [1921] that using a Nicol prism 'serves to cut off a great deal of the blue atmospheric "haze" which usually envelops a distant view, and mostly consists of polarized light.' Although the reason for the color and polarization of the sky had been explained some time before by J. W. Strutt [1871], later Lord Rayleigh, and the neutral points, where the polarization of the sky becomes zero, had already been named after their discoverers Arago [Barral, 1858], Babinet [1840] and Brewster [1842], this simple observation of Raman's was still considered noteworthy, because of the difference between the behavior of the object being observed and the haze. The reason for this difference is that light scattered by molecules and small aerosol is strongly polarized in a plane perpendicular to the scattering plane (the plane defined by the sun, the object being viewed and the observer) while light scattered by surfaces is only weakly polarized. Thus, when Raman oriented the polarizer to transmit light in the plane parallel to the scattering plane the contributions from light scattered by aerosols and molecules were suppressed while the lighthouse was made more visible (had more contrast). This difference between the polarizing properties of aerosols and molecules as compared to surfaces is used by modern polarimetric remote sensing instruments to determine the amount, size and type of aerosols that are present above the surface.

There are therefore three facets to the use of downward-looking polarimetric measurements for the remote sensing of aerosols over land surfaces. A method for the measurement of the polarization of the scene being observed, a quantitative model of the polarized reflectance behavior of the underlying surface and an understanding of what aspects of the aerosol loading, microphysics and vertical distribution are revealed in the polarization signal. This chapter is therefore organized as follows. In Section 2 we provide a brief review of the different instrumental approaches that have been taken to the Earth viewing measurement of polarization. This review focuses on the benefits and issues related to these measurement techniques with particular regard to their use over land. In Section 3 we summarize the conclusions that have been drawn in the existing literature related to the polarized reflectance of land surfaces and discuss how various modeling approaches, that can be used in remote sensing applications, take advantage of the polarized behavior of the surface. Although single scattering models of the polarized light reflected by the atmosphere–surface system of the Earth have been used with considerable success [Deschamps et al., 1994, Deuzé et al., 2001], when measurements are of sufficient accuracy, or extend into the blue, or ultraviolet spectral domain it is not sufficient to use such an approach for the modeling of the observed polarized radiances. In Section 4 we therefore describe how

the land surface–atmosphere system can be modeled with different levels of fidelity depending on the accuracy and spectral domain of the measurements that are available. In Section 5 we review existing retrieval methods [Deuzé et al., 2001] and discuss how optimal methods [Rodgers, 2000; Dubovik and King, 2000] can be applied in the case of polarimetric remote sensing [Hasekamp and Landgraf, 2007, Lebsock et al., 2007]. In particular we emphasize the capability provided by the extended spectral range and more accurate measurements that are currently available in airborne polarimeters and are expected to be available in future spaceborne instruments.

2. Measuring polarization

In order to discuss how different instrument concepts implement the measurement of polarization we will define here the Stokes vector of light and how it is related to a simple measurement system [Hansen and Travis, 1974]. The intensity and polarization of light can be described by the Stokes vector $\boldsymbol{I}^T = (I;\ Q;\ U;\ V)$ where I is a measure of the intensity of the light, Q and U define the magnitude and orientation of the linearly polarized fraction of the light and V is a measure of the magnitude and helicity of the circular polarization. All four Stokes vector elements have the dimensions of intensity (e.g., W m^{-2} and have a simple relation to the time-averaged electric field of a superposition of transverse electromagnetic waves propagating in the same direction.

All four of the Stokes parameters describing a beam of light can be measured using a detector that is sensitive only to the intensity by first transforming the incident beam of light with a retarder and then using a polarizer to analyze the polarization state. The intensity that is observed by such a detector is given by the expression,

$$I(\theta,\delta) = \frac{1}{2}[I + Q\ \cos 2\theta + (U\ \cos\delta + V\sin\delta)\ \sin 2\theta], \tag{1}$$

in which δ is the relative phase delay between the electric vectors in orthogonal planes (E_x and E_y) and θ is the angle of rotation of the polarizer with respect to the x-plane. It is clear that by carefully choosing four measurement pairs δ and θ, the four Stokes parameters can be calculated. For the sake of discussing the instrumental issues involved in making polarization measurements it is worth examining a simple pair of measurements made by a detector with a polarizer in front of it that is oriented at 0° and then 90°. Using Eq. (1) the relevant expressions are seen to be

$$\left.\begin{array}{l} I(90,0) = (I+Q)/2 \\ I(90,0) = (I-Q)/2 \end{array}\right\} \quad \Rightarrow \quad \left\{\begin{array}{l} I = [I(0^\circ,0^\circ) + I(90^\circ,0^\circ)]\ /2 \\ Q = [I(0^\circ,0^\circ) - I(90^\circ,0^\circ)]/2 \end{array}\right. . \tag{2}$$

The main difficulty in ensuring that the measurement of the Stokes vector component, Q, is accurate is that, for most Earth scenes, it is at least an order of magnitude smaller than the intensity, I. Operationally, in this case, it is therefore determined as the small difference between two large numbers. The reason for this is that the contribution to the Stokes vector element I by reflectance over land, is much larger than the contribution to the Stokes vector elements Q and U. This means that if there is a small error in either, or both, measurements

there will be a large fractional error in the estimate of Q, even though the fractional error in the estimate of the intensity, I, might be quite small. Clearly if the 0° and 90° observations are made of slightly different scenes either through spatial mismatch, or a time delay between measurements there is the potential to create significant errors in the estimated Stokes vector elements and it is these errors that are usually called false polarization errors.

We have presented a very specific example here, but examining Eq. (1) it is apparent that any method for estimating Q, U and V will require the use of differences, or some form of modulation of a polarizer or a retarder and that in all of these schemes the intensity is a large static or invariant term that is the most readily estimated. The determination of Q, U and V is therefore a test of the capability of a polarimeter to accurately determine a small modulation, or difference, in the presence of a large background signal.

In the following subsections we describe polarimeter designs that use oriented polarizers [Deschamps et al., 1994; Cairns et al., 1999], temporal modulation of retarders [Diner et al., 2007] and spectral modulation induced by crystal elements [Jones et al., 2004] in order to measure polarization. In order to fully exploit the information content available from polarimetric observations it also necessary to observe the same scene from multiple angles and we therefore also briefly note how the various sensors using these polarimetric analysis methods achieve this multi-angle sampling. Although we make no claims for the completeness of this set of polarimeters they do represent the three basic methods that have been used, or are planned, for use in measurements of polarization from aircraft, or satellites. We also note that since the amount of sunlight that is circularly polarized by reflection off natural objects, aerosols, or molecules is negligibly small the focus of the Earth observing instruments developed to measure polarization has been on the first three Stokes parameters I, Q and U [Kawata, 1978]. The interactions of incident sunlight with the surface–atmosphere system can therefore be modeled using the upper left three by three block of the atmosphere–surface Mueller reflection matrix [Hansen and Travis, 1974].

2.1 Oriented polarizers

The two instruments that have provided most of the downward-looking measurements of the polarization of the Earth and its atmosphere and that have been used in the remote sensing retrieval of aerosol properties are the Polarization and Directionality of the Earth Reflectance (POLDER) sensor [Deschamps et al., 1994] and the Research Scanning Polarimeter (RSP) [Cairns et al., 1999]. The POLDER sensor has flown on three satellite missions, ADEOS I, ADEOS II and PARASOL while the RSP has flown on four different types of aircraft in a number of large field experiments. The NASA Glory mission [Mishchenko et al., 2007], scheduled for launch in June 2009, will also carry a polarimeter, the Aerosol Polarimetry Sensor (APS), which uses the same conceptual design as the RSP. Both the POLDER and RSP use oriented polarizers to analyze the polarization state of incident radiation. However the way in which they do this is substantially different with the POLDER instrument using a sequential rotation of polarizers while the RSP measures the intensity in four polarization orientations in multiple spectral bands simultaneously. There are benefits and costs to each approach and we therefore describe them separately.

2.1.1 Sequential measurement

The simplest way to estimate the first three Stokes vector elements of a scene is to rotate a polarizer in front of a detector. This method is the basis of the POLDER instrument that measures the linear polarization state of light in three spectral bands at 443, 673 and 865 nm using polarizers that are sequentially oriented at 0°, 60° and 120°. The POLDER instrument also makes intensity only measurements in a number of other bands and provides images of the scene being viewed on a two-dimensional (2D) charge-couple device (CCD) array. The Stokes parameters I, Q and U can be determined from the three sequential polarizer measurements using the formulae

$$\begin{aligned} I &= \frac{2}{3}[I(0^\circ,0^\circ) + I(60^\circ,0^\circ) + I(120^\circ,0^\circ)], \\ Q &= \frac{2}{3}\{[I(0^\circ,0^\circ) - I(60^\circ,0^\circ)] + [I(0^\circ,0^\circ) - I(120^\circ,0^\circ)]\}, \\ U &= \frac{2}{\sqrt{3}}[I(60^\circ,0^\circ) - I(120^\circ,0^\circ)]. \end{aligned} \tag{3}$$

The frame rate of POLDER is sufficiently high that multiple images are captured of every pixel providing multi-angle views of the same scene. However, as the satellite flies over the Earth the scene that is being viewed moves across the focal plane array as the polarizers with different orientations sequentially analyze the scene being viewed. In order to minimize the errors that are caused by this motion, the POLDER sensor uses a motion-compensation plate to provide the best possible spatial matching of the different scenes that are viewed with the polarizers in their different orientations. This is difficult to achieve over the full field of a wide-angle camera such as POLDER and not even possible if there are actual time variations in the scene being observed, such as when there are moving clouds within a pixel. As we note above, false polarization is a concern for sequential, or spatially mismatched measurements, and the consequent uncertainty in the estimates of Q and U that POLDER provides are expected to be of the order of 1–2 % larger than for I over heterogeneous surfaces [Hagolle et al., 1999], with better accuracy possible over homogeneous surfaces such as the open ocean. Nonetheless the POLDER instrument has demonstrated that an instrument of this kind has a valuable capability to retrieve aerosol properties over land and one that is not as sensitive to the underlying surface as sensors that only use reflectance measurements [Deuzé et al., 2001; Fan et al., 2008], as we will discuss in Section 4.

2.1.2 Simultaneous measurements

Wollaston prisms are optical elements that when illuminated by a collimated incident beam provide angular separation, and consequently spatial separation, of the beam into orthogonal polarization states. They can therefore be used, when combined with an optical system such as a relay telescope, to measure two orthogonal polarization states of the same scene simultaneously, eliminating false polarization from the estimate of the Stokes vector parameters. The RSP uses a refractive relay telescope to define the field of view and provide collimated illumination of a Wollaston prism that spatially separates beams with

orthogonal polarization states that then illuminate paired detectors. By making measurements with one telescope in which the Wollaston prism is oriented to analyze orthogonal polarization states of 0° and 90° (see Eq. (2)) and with a second telescope in which the Wollaston prism is oriented to analyze orthogonal polarization states of 45° and 135° the RSP allows all three Stokes parameters, I, Q and U, to be determined simultaneously. Wollaston prisms are broadband optical elements and this allows the RSP design to use each telescope to make measurements in three spectral bands that are separated by dichroic beam splitters. There are a total of six telescopes in the RSP. Three of the telescopes measure the Stokes parameters I and Q in nine spectral bands, while the other three telescopes measure the Stokes parameters I and U in the same nine spectral bands providing simultaneous measurements of I, Q and U in all nine spectral bands. The nine spectral bands are at 410, 470 (443), 555, 670, 865, 960 (910), 1590, 1880 (1378) and 2250 nm. The three spectral band centers in parentheses are those that will be used for the Aerosol Polarimetry Sensor that are different from the RSP. The band at 443 nm will be used for APS because it is better for ocean color estimation, is darker over land and is less affected by trace gas absorption than the RSP 470 nm band. The band at 910 nm will be used for APS because it provides a broader dynamic range for water vapor estimates than the RSP band at 96 nm and allows for better detector performance when using silicon detectors. Both the 1378 and 1880 nm bands are extremely effective for screening for thin cirrus clouds, but in the event of a volcanic eruption the shorter wavelength 1378 nm band would allow for better detection and characterization of stratospheric aerosols and so this band was chosen for the APS. The instantaneous field of view (14 mrad) of each telescope is scanned continuously, with data being taken over a view-angle range of 120° (± 60° from nadir), using a polarization-insensitive scan mirror system. This system consists of two mirrors each operating with a 45° angle of incidence with their planes of incidence oriented orthogonally. This ensures that the polarization orientation that is perpendicular to the plane of reflection at the first mirror is parallel to the plane of reflection at the second mirror so that all polarization states are transmitted equally. The scan is oriented along the aircraft, or satellite, ground track in order to provide multiple views of the same scene from multiple angles. The RSP also incorporates a calibration system that allows the relative responsivity of the detectors measuring orthogonal polarization states to be tracked continuously allowing a polarimetric accuracy of better than 0.2 % [Cairns et al., 1999] to be achieved independent of the scene that is being viewed.

2.2 Temporal modulation

As can be seen from Eq. (1) varying the retardance of an element that is then followed by a polarizer at a fixed angle also allows the incident polarization state of a beam of light to be analyzed. A practical implementation of this concept, that is somewhat more complicated than the simple system modeled by Eq. (1), is to use a photo-elastic modulator (PEM) to provide a time-varying retardance that is placed between a pair of quarter-wave plates such that the combination acts as a time-varying circular retarder [Chipman, 1994]. The circular retarder modulates Q and U such that if it is followed by an appropriately oriented polarization analyzer and detector the temporal modulation of the detector signal is well represented by the formula,

$$I(0^\circ, \delta) = \frac{1}{2}(I + Q\ \cos\delta + U\ \sin\delta). \tag{4}$$

In astronomical applications it is feasible to use high-speed demodulation at the resonant frequency (typically between 10 and 100 kHz) and harmonics of the PEM in order to determine Q and U using the different phase and harmonic content of their modulation [Keller, 2002; Povel et al., 1990]. For Earth remote sensing applications this is an extremely high speed at which to operate a focal plane, given that the frame rate of a push broom imager with a resolution of hundreds of meters in low Earth orbit is expected to be on the order of tens of milliseconds. An ingenious approach to imaging polarimetry for Earth-viewing satellite applications has therefore been proposed in which a pair of PEMs are used as the source of retardance modulation with the analysis of the signal being performed at the beat frequency [Diner et al., 2007]. In this method analyzers oriented at 0° and 45° are used to provide estimates of I, Q and U as indicated in the following equations:

$$\begin{aligned} I(0^\circ, \delta_b) &= 1/2[I + QJ_0(\delta_b)], \\ I(45^\circ, \delta_b) &= 1/2[I + UJ_0(\delta_b)], \end{aligned} \tag{5}$$

in which J_0 is the zero-order Bessel function and the effective magnitude of the beat frequency retardance modulation, δ_b, is

$$\delta_b = 2\delta_0\ \cos(\omega_b t - \eta), \tag{6}$$

with ω_b being the beat frequency, η the phase difference between the modulating waveforms of the two PEMs, δ_0 is the magnitude of the retardance modulation of a single PEM and t is time. Although 'false'' polarization can contaminate the estimate of Stokes vector elements using this measurement approach it is expected to be a weak effect since only temporal variations in the scene that are similar to the terms modulating Q and U will alias into those elements. This polarimetric concept is being implemented as an imaging polarimeter in which a push broom imaging mode provides cross-track coverage while multi-angle views are obtained by the brute force approach of having individual cameras for each view angle. The polarimetric analysis concept underlying this measurement approach has been demonstrated by a laboratory prototype [Diner et al., 2007] but has not, thus far, been used for remote sensing measurements.

2.3 Spectral modulation

The final approach to remote sensing measurements of polarization that we review here has only been developed recently. It uses spectral modulation to encode the Stokes vector into an intensity measurement [Jones et al., 2004; Oka and Kato, 1999]. In this method a system of polarization analysis optics is inserted between the scene being viewed and an imaging spectrometer. These polarization analysis systems have the advantage, for implementation in a remote sensing system, that they have no moving parts. The way that they work is by imposing a variation on the incident spectrum that is rapid (hyperspectral) compared with the spectral variations of atmospheric aerosol and molecular scattering. This rapid variation depends on the Stokes vector, with one particular implementation being described by Eq. (7),

$$I(v) = 1/2[I + Q\ \cos(\phi)] + 1/4U[\cos(\Delta\phi) - \cos(\Sigma\phi)] + V[\sin(\Sigma\phi) - \sin(\Delta\phi)], \quad (7)$$

where the modulating terms in the sinusoids are

$$\begin{aligned} \phi &= 2\pi v(n_e - n_o)l_2/c, \\ \Delta\phi &= 2\pi v(n_e - n_o)(l_1 - l_2)/c, \\ \Sigma\phi &= 2\pi v(n_e - n_o)(l_1 + l_2)/c, \end{aligned} \quad (8)$$

with l_1 and l_2 being the optical path lengths through two birefringent crystal elements that compose the polarization analysis optics and n_e and n_o being the refractive indices for the extraordinary and the ordinary rays in those crystals. The frequency and speed of light are represented by v and c respectively. Since the modulating terms are 'fast' compared to variations in atmospheric scattering the Stokes vector can be estimated within broader windows (typically of 10–20 nm) over the entire spectrum that is measured by the imaging spectrometer. Multi-angle views can be provided along the ground track of a plane, or satellite, by orienting the image direction of the imaging spectrometer in the direction of motion. In principle this is a robust and accurate way to estimate the Stokes vector since there are no moving parts and the Stokes vector elements are all encoded onto the spectrum simultaneously. These measurements are therefore inherently insensitive to 'false' polarization caused by temporal or spatial variations in the scene intensity that is observed being aliased into the estimated polarization state. Of course since the polarization state is modulated onto the spectrum, care must be taken to avoid, or correct for atmospheric absorption or scattering features that could themselves cause 'false' polarization [Jones et al., 2004]. In practice, as with all accurate measurement systems, great care needs to be taken to ensure the thermal and mechanical stability of the system so that it can be characterized and calibrated on the ground in a way that is applicable to the remote sensing measurements themselves. A remote sensing instrument that uses hyperspectral modulation (Hyperspectral Polarimeter for Aerosol Retrievals HySPAR) has been developed and successfully flown [Jones et al., 2004], and although the scientific analysis of the data obtained is still in its early phases the comparisons of the degree of linear polarization ($DoLP = \sqrt{(Q^2 + U^2)}/I$) with simultaneous RSP measurements showed reasonable (within a few percent) agreement, given that this was one of the first flights of this sensor.

3. Surface polarization

In the following discussion we will refer frequently to the polarized reflectance because it is a particularly useful quantity to use in discussing the polarizing properties of surfaces. This is a result of its simplicity, in terms of representing polarization properties, and also in understanding why those properties behave the way they do. The solutions to multiple scattering problems and the effects of surface reflection on arbitrary radiation fields can be conveniently expressed as reflection matrices, **R**, each composed of four rows and four columns such that

$$\mathbf{I}_v(\mu_v, \varphi_v) = \frac{1}{\pi}\int_0^1 \mu_s\ \mathrm{d}\mu_s \int_0^{2\pi} \mathrm{d}\varphi_s \mathbf{R}(\mu_v, \mu_s; \varphi_s - \varphi_v)\mathbf{I}_s(\mu_s, \varphi_s), \quad (9)$$

where μ and φ are the cosine of the zenith angle and the azimuth angle, with the subscripts s and v indicating that the angles referred to are the direction of the source radiation and the viewing direction respectively. It is assumed here that there is no preferred direction so that the only azimuthal dependence of the reflection matrices is on the difference between the solar and view azimuths, $\Delta\varphi = \varphi_s - \varphi_v$. The Stokes vector $\mathbf{I}_\eta$ describes the source of radiation incident from the top on the surface, or surface-atmosphere system, represented by its reflection matrix, $\mathbf{R}$, and v is the Stokes vector of the reflected radiation field that is being observed. For the purposes of this discussion the source of radiation is the sun which is essentially unpolarized, at least in terms of the average value across the solar disk, and for which the Stokes vector is well approximated by the expression $\mathbf{I}_s^T = [F_s\delta(\mu - \mu_s)\delta(\phi - \phi_s), 0, 0, 0]$ where the Greek delta symbol is used to represent the Dirac delta function and F_s is the solar irradiance at the top of the atmosphere. Substituting the particular behavior of the Stokes vector of the solar radiation into Eq. (9) yields the formula,

$$\mathbf{I}(\mu_v, \varphi_v) = \frac{\mu_s F_s}{\pi} \begin{pmatrix} R_{11}(\mu_v, \mu_s; \Delta\varphi) \\ R_{21}(\mu_v, \mu_s; \Delta\varphi) \\ R_{31}(\mu_v, \mu_s; \Delta\varphi) \\ R_{41}(\mu_v, \mu_s; \Delta\varphi) \end{pmatrix} \tag{10a}$$

and the complementary relations that define the reflectances in terms of the Stokes parameters

$$\begin{pmatrix} R_{11} \\ R_{21} \\ R_{31} \\ R_{41} \end{pmatrix} = \begin{pmatrix} \frac{\pi I}{\mu_s F_s} \\ \frac{\pi Q}{\mu_s F_s} \\ \frac{\pi U}{\mu_s F_s} \\ \frac{\pi V}{\mu_s F_s} \end{pmatrix}. \tag{10b}$$

Since the circular polarization is negligibly small [18] the magnitude of the polarized reflectance, R_p, can therefore be defined to be

$$R_p = \pm\sqrt{R_{21}^2 + R_{31}^2}, \tag{11}$$

which, like the usual definition of reflection, has the benefit that it is independent of the brightness of the illuminating source. This expression does not capture the orientation of the polarization, but for single scattering the polarization is either parallel to or perpendicular to the plane of scattering (the plane that contains the solar and viewing directions). Therefore, if the polarized radiance is defined to be positive when the polarization direction is perpendicular to the plane of scattering and negative when it is parallel to the plane of scattering, all of the information in the polarized reflectance is captured by the polarized reflectance defined in Eq. (9). It has also been found that, even for multiple scattering, rotating the reference frame for Q and U into the scattering plane causes U to become small, with the predominant information content of the observations being captured by Q. Thus, calculating the polarized reflectance using Eq. (11) with a sign that is assigned based on whether Q in the scattering plane is positive, or negative, captures the majority of the information in polarization measurements without recourse to multi-dimensional vec-

tors. We do note, however, that the best accuracy can be retained, when actually performing calculations or retrievals, by using the Stokes vector elements themselves.

One of the main beauties of the Earth when viewed in remote sensing measurements from space, or aircraft, is its bright, many-hued underlying surface. This also presents one of the main difficulties in retrieving aerosol amounts and types using passive remote sensing measurements of the intensity over land surfaces, as noted elsewhere in this volume, since the background is brighter than our object of interest, the aerosols in the atmosphere. Although the polarized reflectance of the land surface at visible wavelengths is typically smaller than the signal from aerosols, it is clear that in order to use polarization measurements to provide an accurate determination of the type and amount of aerosols present in the atmosphere we need a quantitative understanding of the polarization properties of the land surface. Such a quantitative understanding, though not the subject of this discussion, would also be of use in remote sensing of the surface, being indicative of the texture of soils, or the leaf inclination distribution of vegetation. Fig. 10.1 shows an image of the different behavior of reflectance and polarized reflectance. The strong contrast between vegetated and bare fields shown by the reflectance image (Fig. 10.1, left panel) is absent in the polarized reflectance image (Fig. 10.1, right panel) which shows the dependence of

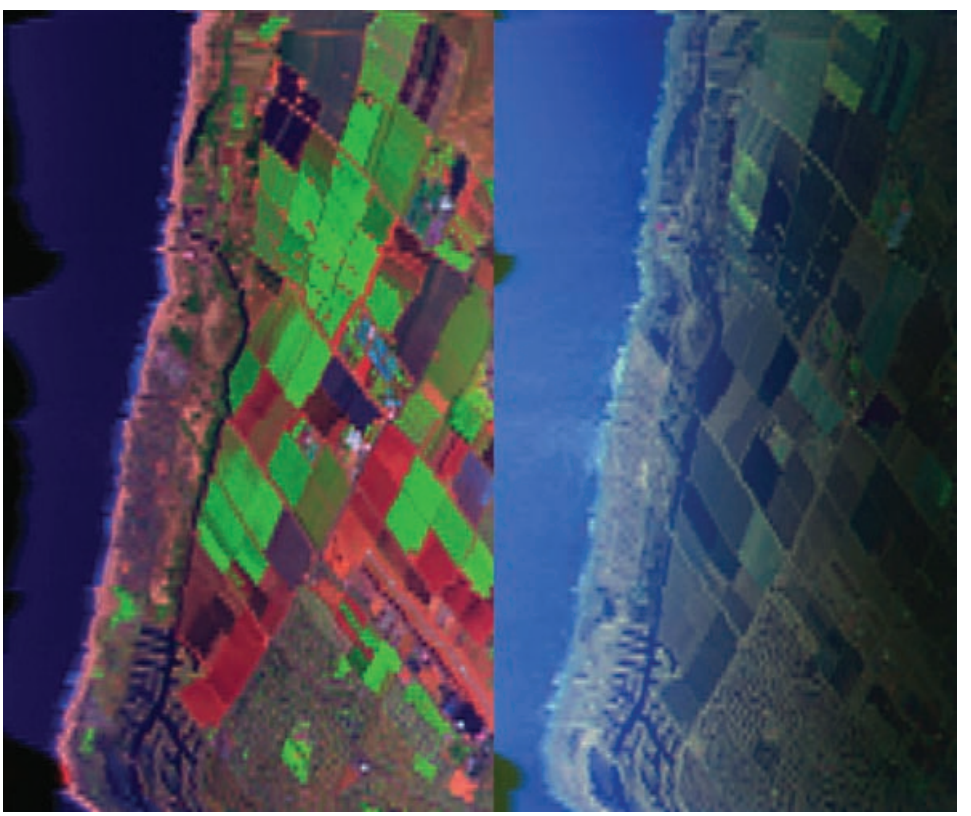

Fig. 10.1. False-color images created using RSP observations obtained on an aircraft flying at 3000 m above Oxnard and Ventura, California, USA. The red, green and blue colors are the 2250, 865 and 410 nm reflectances (left) and polarized reflectances (right) respectively.

molecular scattering on viewing geometry, decreasing from left to right with scan angle as the scattering angle increases from near 90° towards the backscattering direction.

The polarizing properties of natural surfaces as understood from ground- and aircraft-based measurements and observations from several space shuttle flights have been summarized by Coulson [1988]. This summary is still an excellent reference to the historical measurements that have been made of the polarizing properties of mineral and vegetated surfaces, although the tendency to present linear polarization measurements in terms of the *DoLP* makes some of this information difficult to use. This is because the *DoLP*, which is a ratio, mixes the effects of the polarization properties of the surface (numerator) and the reflection properties of the surface (denominator) that are to a large extent caused by the different mechanisms of surface and volume scattering respectively. There have also been a significant number of satellite measurements provided by the POLDER sensor flown on the ADEOS-I, -II and PARASOL missions, and airborne measurements made by the RSP sensor since Coulson's review was published. In this Section we will therefore present the understanding of the polarizing properties of the surface that has been developed based on these more recent measurements, together with the historical measurements, and how the surface polarized reflectance can therefore be modeled.

Our current understanding is that the polarization of surfaces is primarily generated by external reflections off the facets of soil grains, or the cuticles of leaves. A consequence of this surface polarization being generated by external reflections is that its magnitude will tend to be spectrally neutral as long as the real refractive index of the surface varies little. This is generally true of both minerals [Pollack et al., 1973] and the surface cuticles of

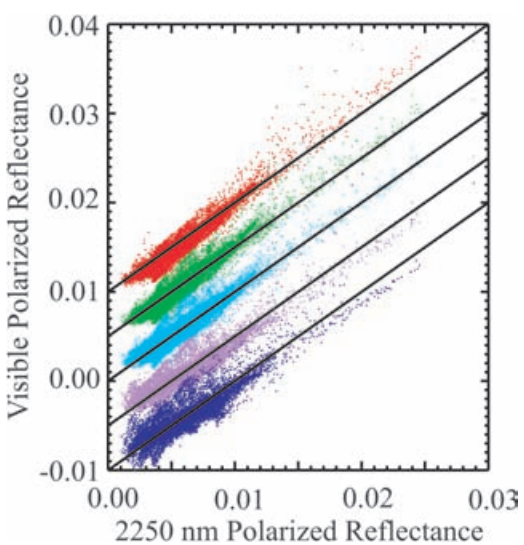

Fig. 10.2. Polarized reflectance measurements taken with the RSP sensor mounted on a small survey plane over agricultural land near Oxnard, California, USA, at an altitude of 3000 m. The visible polarized reflectances at 410, 470, 555, 670 and 865 nm are plotted against that at 2250 nm in blue, mauve, turquoise, green and red respectively. The bands are offset by 0.005 from one another to allow any spectral differences in behavior to be identified. The solid (1:1) lines show what is expected if the surface has a gray polarized reflectance.

vegetation [Vanderbilt et al., 1985; Rondeaux and Herman, 1991] and has been experimentally verified to be true for forests, bare soils, agricultural fields and urban landscapes over the spectral range from the deep blue to the infrared. Thus, although the surface reflectance is both colorful and spatially variable, the surface polarized reflectance is spatially variable but spectrally gray. It is this feature of the surface polarized reflectance that makes polarization measurements such a useful tool for aerosol retrievals over land. The key remaining questions regarding the surface polarized reflectance, if we are to use polarization for remote sensing of aerosols, are the predictability of its absolute value, for a particular surface, and its angular distribution.

Measurements taken with the RSP sensor over agricultural land containing bare soil and a range of different crops that are grown near Oxnard, CA (broccoli, peppers etc.) are shown in Fig. 10.2. This provides an example of the absence of spectral variability that is seen in the observed polarized reflectance for a wide range of viewing geometries and surface types. These measurements, which were obtained with the RSP installed in a small survey plane flying at an altitude of 3000 m, have been atmospherically corrected using simultaneous, collocated sunphotometer measurements. In Fig. 10.3 we show the angular variation of the polarized reflectance separately for soil (ploughed fields) and vegetation (soy bean, or winter wheat fields) in the Southern Great Plains of the United States (during the ALIVE field experiment) and over the Dismal Swamp in Virginia (during the CLAMS field experiment). Although the two surface types have different magnitudes of polarized reflectance they both have spectrally neutral polarized reflectance as evidenced in the residual differences between all the shorter wavelength channels and the longest RSP channel at 2250 nm shown in the lower parts of Figs 10.3(a) and (b). They also show a similar functional variation with view angle. These surface reflectance estimates

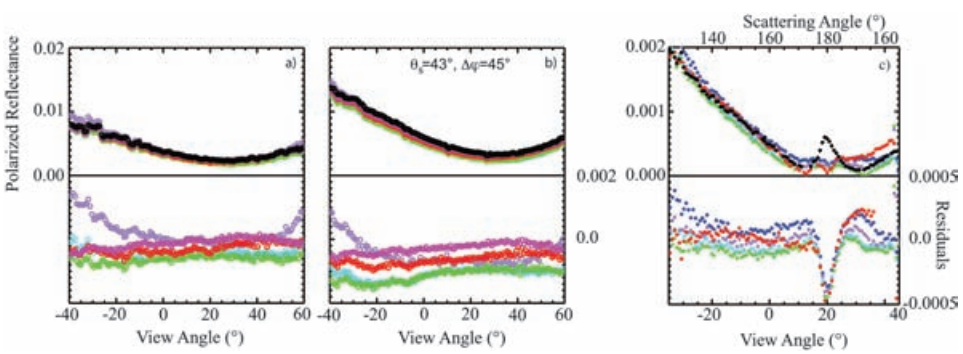

Fig. 10.3. Polarized reflectance measurements taken with the RSP sensor (mounted on the Sky Research Inc. BAE J-31 research plane) at an altitude of 200 m above the Southern Great Plains in Oklahoma (a) and (b) during the ALIVE field experiment. For (a) and (b) the solar zenith angle (θ_s) is 43° and the relative solar azimuth angle ($\Delta\varphi$) is 45°. The data in (c) was obtained with the RSP sensor on a Cessna 310 at 200 m over the Dismal Swamp in Virginia during the CLAMS field experiment; the solar zenith angle was 20° and the relative solar azimuth angle is less than 1°. The measurements were atmospherically corrected and have been separated into vegetated (a), bare soil (b) and (c) forested swamp surface types with the bands at 410, 470, 555, 670, 865, 1590 and 2250 shown in blue, mauve, turquoise, green, red, purple and black respectively. The residuals are the differences between the polarized reflectance at 2250 nm and the polarized reflectance in each of the other bands, using the same color scheme as used for the polarized reflectances figures.

are based on measurements that were taken at 200 m above the surface and that were corrected to the surface level using data from a nearby ground-based sunphotometer [Holben et al., 1998] and a sunphotometer on top of the aircraft [Redemann et al., 2006] to define the aerosol scattering and a microwave radiometer to define the amount of water vapor present. Other surfaces such as swamps, cityscapes and forests (not shown) show similar behavior with little spectral variation in the surface polarization.

These measurements show that if a long-wavelength measurement (e.g., 2200 nm) that is only weakly affected by the aerosol and molecular scattering is available then this can be used to characterize the polarized reflectance across the entire solar spectrum. A similar concept has been put forth for the retrieval of aerosols over land using radiance measurements in a more limited set of spectral bands [Kaufman et al., 1997]. The only limiting factor in using a long-wavelength measurement to characterize the surface is whether the observational viewing geometry is sufficient to predict the behavior of the surface polarization for other viewing geometries. This is primarily of concern for short wavelengths where the molecular and aerosol scattering is sufficiently strong that diffuse surface–atmosphere interactions do have to be modeled. When diffuse interactions are significant a substantial fraction of the radiation incident at the surface is not in the direction of the direct solar beam and a substantial fraction of the observed radiation was not reflected by the surface into the viewing angle. This is why a model of the surface is necessary for accurate forward modeling of the observed polarized reflectance at short wavelengths. In Fig. 10.4 we show an observation in the solar principal plane (the plane that contains the local vertical and the sun) that is used to estimate the parameters in a simple Fresnel model of the surface polarized reflectance, viz.

$$R_p^{Surf}(\mu_s, \mu_v, \Delta\varphi) = \zeta R_p^F(\gamma). \tag{12}$$

R_p^F is the Fresnel coefficient for polarized light calculated for a surface refractive index of 1.5.γ is the reflection angle that can be expressed as a function of the scattering angle $\Theta = \mathrm{acos}[-\mu_v\mu_s + \sqrt{(1-\mu_v)^2(1-\mu_s)^2}\cos(\phi_v - \phi_s)]$ by $\gamma = \pi - \Theta/2$ with ζ being a coefficient that provides the best fit to the measurements at 2250 nm in the solar principal plane. This model assumes that the surface does not have a preferred azimuth, as a ploughed field would have for example, and is therefore applicable to natural surfaces, or urban landscapes over a sufficiently large area that this assumption is valid. The model is then used to predict the polarized reflectance of this surface in a different scan plane from the original observations. It can be seen that the model prediction of the polarized reflectance for a different viewing geometry to that used to estimate the model is in good agreement with the observations in this other scan plane. The conclusion we draw is that a simple Fresnel model, fitted to observations of the surface (or long-wavelength observations), is sufficient to predict the angular variation of the surface polarized reflectance at all view angles that are not close to the backscatter direction.

When a long-wavelength measurement is not available it is necessary to predict the magnitude of the surface polarized reflectance using other observations, or prior information in order to use polarization measurements for remote sensing of aerosols. If the polarized reflectance of vegetation showed the same magnitude of variability as the polarized reflectance at Brewster's angle that is seen in single leaves [Grant et al., 1993], it unlikely that such an approach would work. However, the variability in the polarized reflectance

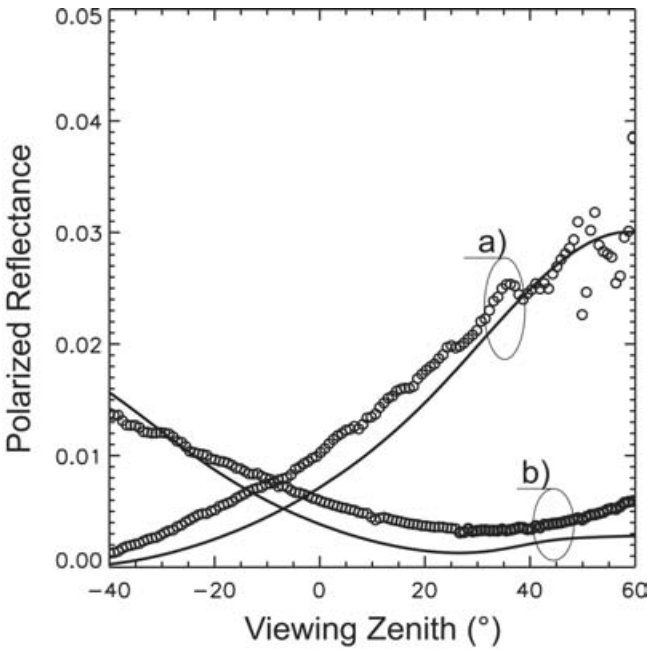

Fig. 10.4. Atmospherically corrected polarized reflectance measurements at 2250 nm with the data taken in meridional planes (a) close to the principal plane (b) at 45° to the principal plane.

between different plant types is not that great, which indicates that the macroscopic behavior of plant canopies, or ensembles is not well represented by measurements of individual leaves at a single angle. A more important predictor of the polarized reflectance of surfaces is the fractional coverage of vegetation and soil, since the differences between the polarized reflectance of soils and vegetation are larger than the variability within either class (see Fig. 10.2). This property of the surface polarized reflectance was used in an analysis of POLDER data [Nadal and Bréon, 1999] to generate a model that is only dependent on the surface type and the normalized difference vegetation index (NDVI) [Tucker, 1979]. The NDVI serves as a proxy for the fractional coverage of soil and vegetation, while the partitioning of the POLDER data into different surface types allows the model, viz.

$$R_p^{Surf}(\mu_s, \mu_v, \Delta\varphi) = a_0 \left[1 - \exp\left(-\frac{\beta_0 R_p^F(\gamma)}{(\mu_s + \mu_v)} \right) \right], \tag{13}$$

to account for the fact that NDVI depends both on fractional coverage of vegetation and vegetation type by allowing the parameters a_0 and β_0 to be different for the various surface types of the International Geosphere–Biosphere Program classification [Belward et al., 1999]. This surface model has been successfully used in the operational processing of POLDER data for the retrieval of aerosol properties over land [Deuzé et al., 2001], although it has been found that the retrievals are affected by errors in the model prediction of surface polarized reflectance [Waquet et al., 2007]. This model limits the magnitude of polarized reflectance, at high view and solar zenith angles when the argument of the ex-

ponent in Eq. (13) is large to a_0. At lower view and zenith angles the exponent in Eq. (13) is small and the surface polarization can be approximated, by the expression

$$R_p^{Surf}(\mu_s, \mu_v, \Delta\varphi) \approx \frac{a_0 \beta_0 R_p^F(\gamma)}{(\mu_s + \mu_v)}, \tag{14}$$

which is similar to the vegetation model proposed by Breon et al. [1995] with a scaling factor of $a_0\beta_0$ that plays the same role as ζ in Eq. (12), although the dependence on view and zenith angles of Eqs (12) and (14) is different.

4. Modelling atmosphere–surface interactions

In this Section we describe how the surface models introduced above can be incorporated into a radiative model of how the atmosphere and surface interact. It is forward models of this kind that are then used either in optimal estimation, or look-up-table (LUT) approaches, to perform the aerosol retrievals that are described in Section 5. In order to describe the main processes that generate the up-welling polarized reflectance, we provide in Eq. (15) an approximate expression for the surface–atmosphere Mueller reflection matrix, viz.

$$\mathbf{R}^{Atm+Surf} = \mathbf{R}^{Atm} + t_+ \mathbf{R}^{Surf} t_- + \left[\mathbf{T}_+^d \mathbf{R}^{Surf} t_- + t_+ \mathbf{R}^{Surf} \mathbf{T}_-^d + \mathbf{T}_+^d \mathbf{R}^{Surf} \mathbf{T}_-^d\right], \tag{15}$$

in which we have suppressed the dependence of the matrices on the viewing geometry $(\mu_s,\ \mu_v\varphi_s - \varphi_v)$ and wavelength for the sake of clarity. The plus (minus) subscripts refer to a downward (upward) direction. $\mathbf{R}^{Atm}$ and $\mathbf{R}^{Surf}$ are respectively the atmospheric and surface reflection matrices. $\mathbf{T}^d$ corresponds to the diffuse transmission matrix of the atmosphere and t is a direct transmission term given by

$$t_{-,+} = \exp\left[-\left(\frac{\tau_{a,\lambda} + \tau_{r,\lambda}}{\mu_{s,v}}\right)\right], \tag{16}$$

where $\tau_{a,\lambda}$ and $\tau_{r,\lambda}$ are respectively the aerosol and molecular total optical thicknesses at a particular wavelength λ.

Eq. (15) separates the terms that contribute to the observed reflectance into three distinct components. The first term $\mathbf{R}^{Atm}$ describes the contribution of the upwelling light scattered from the atmosphere without interactions with the surface. The second term describes the surface contribution transmitted directly through the atmosphere while the third term, between brackets, models the diffuse interactions between the surface and the atmosphere. An exact expression for $\mathbf{R}^{Atm+Surf}$ would require the inclusion of multiple surface reflections (i.e. multiple scattering interactions between surface and atmosphere).

Fig. 10.5 shows an example of polarized reflectances calculated at the top of the atmosphere (TOA) levels (solid lines) and the same quantities calculated when suppressing the process of multiple surface reflections (dots). The effective radius (r_{eff}) and effective variance (v_{eff}) characterize the aerosol size distribution [Hansen and Travis, 1974] and m_r is the refractive index of the aerosols with the calculations being performed for a bimodal

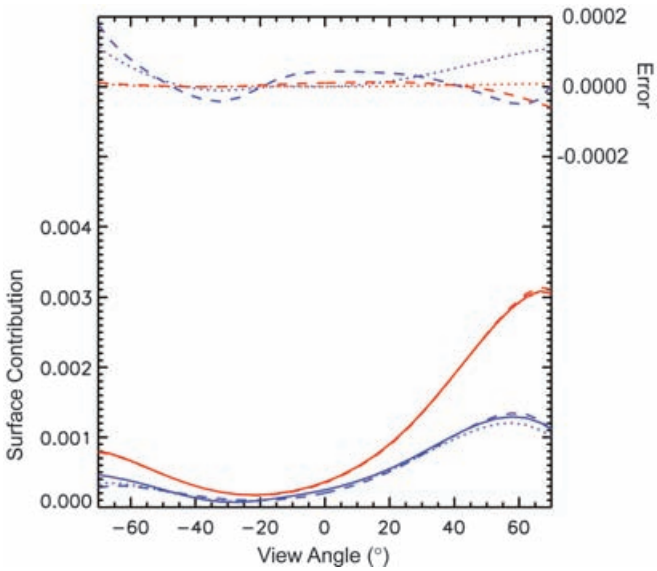

Fig. 10.5. Contribution of the surface to the TOA polarized reflectance at 410 (blue lines) and 865 (red lines) nm: Exact calculations (solid lines), calculations without multiple scattering interactions between surface and atmosphere (dotted lines) and calculations performed using direct transmission term and scaling optical thicknesses (dashed lines). The errors (absolute magnitudes of the difference between exact and approximate calculations) on the surface and TOA polarized reflectances are shown in more detail at the top of the figure. Aerosol layer: $r_{eff=0.14\ \mu m}$, $v^f_{eff} = 0.15$, $r^c_{eff} = 2.5\ \mu m$, $v^c_{eff} = 0.5$, $m^f_r = m^c_r = 1.4$ and $\tau_a = 0.1$ at 550 nm with coarse mode optical depth being 10 % of the total. Calculations made for a solar zenith angle of 30°, $\Delta\varphi = 45°$. The surface albedo was 0.1.

size distribution composed of fine (superscript f) and coarse (superscript c) mode particles. It is apparent that the contribution of multiple surface–atmosphere interactions to the observed polarization at the top of the atmosphere is small. Note that this process is generally accounted for in multiple scattering calculations [Hansen and Travis, 1974] but can, if necessary, be neglected and the surface–atmosphere interaction for polarization can be treated using Eq. (15) rather than an exact calculation.

The polarized reflectance measured over land is usually modeled by considering only the upwelling polarized light scattering from the atmosphere and a single reflection off the surface [Deuzé et al., 2001; Waquet et al., 2007]. The polarized reflectance can then be written in the following form,

$$R^{Calc}_{p,\lambda}(\mu_s, \mu_v, \Delta\varphi) = R^{Atm}_p(\mu_s, \mu_v; \Delta\varphi) + t_-{}^* R^{Surf}_p(\mu_s, \mu_v, \Delta\varphi) t_+{}^*. \tag{17}$$

In this equation R^{Atm}_p is the atmospheric polarized reflectance (i.e. calculation made with a black surface) and R^{Surf}_p is the surface polarized reflectance. $t_{-,+}{}^*$ is a direct transmission term where the aerosol and molecular optical thicknesses are scaled respectively by factors κ and ϕ. These factors are empirically derived and account for the neglect of the diffuse surface–atmosphere interactions [Lafrance, 1997]. In Fig. 10.5, we show the results of using these different approaches to modeling the polarized reflectance at the TOA.

The coefficients κ and ϕ are respectively equal to 0.63 and 0.44. In this example these factors were adjusted to minimize model errors for this particular aerosol model and load over the full range of solar zenith and azimuth angles. Although this approach is optimized, it still introduces some significant errors in the modeling of the surface contribution, resulting in errors in the TOA polarized reflectance that are as large as 0.0001 (2.5 % of the signal). These errors increase at shorter wavelengths for which the diffuse transmission of the atmosphere increases relative to the direct beam transmission.

At these shorter wavelengths, typically less than 670 nm, where the simple model of Eq. (17) is not sufficiently accurate the surface model introduced in Eq. (12) can be used to calculate the surface reflection matrix so that the diffuse interactions between the surface and the atmosphere can be accurately calculated. An approach to modeling the polarized reflectances that has been found to have certain advantages for modeling real data, particular data with high spatial resolution is presented in Eq. (18). For a given viewing geometry, the surface contribution can be calculated by considering only the Fresnel reflectance that is multiplied by a coefficient in order to scale the surface to that which is observed. In practice, this can be implemented model by the formula,

$$R_{p,\lambda}^{Calc} = R_{p,\lambda}^{Atm} + \left[R_{p,\lambda,Fresnel_surface}^{Atm+Surf} - R_{p,\lambda}^{Atm}\right]\xi. \tag{18}$$

The dependence of the quantities on viewing geometry (μ_s, μ_v, $\varphi_s - \varphi_v$) is once again suppressed for clarity. $R_{p,\lambda,Fresnel_surface}^{Atm+Surf}$ is the polarized reflectance calculated when the elements of the reflection matrix are calculated according to the Fresnel law using a surface refractive index equal to 1.5. The term in brackets corresponds to the contribution from surface interactions (see Eq. (15)), which, since multiple surface interactions are negligible (see Fig. 10.5) can simply be multiplied by a scale factor ξ in order to properly include diffuse reflections. The factor ξ that provides an appropriate scaling of the surface reflectance to match the observations is estimated using the formula

$$\xi(\mu_s, \mu_v, \Delta\varphi) = R_{p,2250\text{nm}}^{Meas}(\mu_s, \mu_v, \Delta\varphi) \Big/ R_p^F(\gamma), \tag{19}$$

where R_p^{Meas} is the polarized reflectance measured at 2250 nm. Clearly, if the polarized reflectance at 2250 nm is not affected by aerosols and Fresnel reflectance for a refractive index of 1.5 is a perfect model of the surface then the parameter ξ will be unity and the calculated polarized reflectance will be $R_{p,\lambda,Fresnel_surface}^{Atm+Surf}$ as it should be. Similarly if the actual surface polarized reflectance is negligibly small then ξ will be equal to zero and the calculated polarized reflectance will be simply $R_{p\lambda}^{Atm}$. Eq. (19) is therefore being used to extrapolate from the simple Fresnel model using actual observations of the 2250 nm polarized reflectance. This approach also has the advantage that the scaling factor, ξ, is derived for each view angle and allows for the fact that not all view angles may see exactly the same surface as a result of aircraft attitude variations. For instruments in which the spectral polarization measurements are simultaneously acquired in each view, this modeling allows the surface contribution to be eliminated from the measurements even when different angular samples view different surfaces. This is apparent in Fig. 10.10 (a) where the total polarized reflectance observed with the RSP during ALIVE at an altitude of 4000 m is shown together with the residual errors in the model fit to the data. The large fluctuations in the polarized reflectance (a) are caused by the RSP observing different surface types at

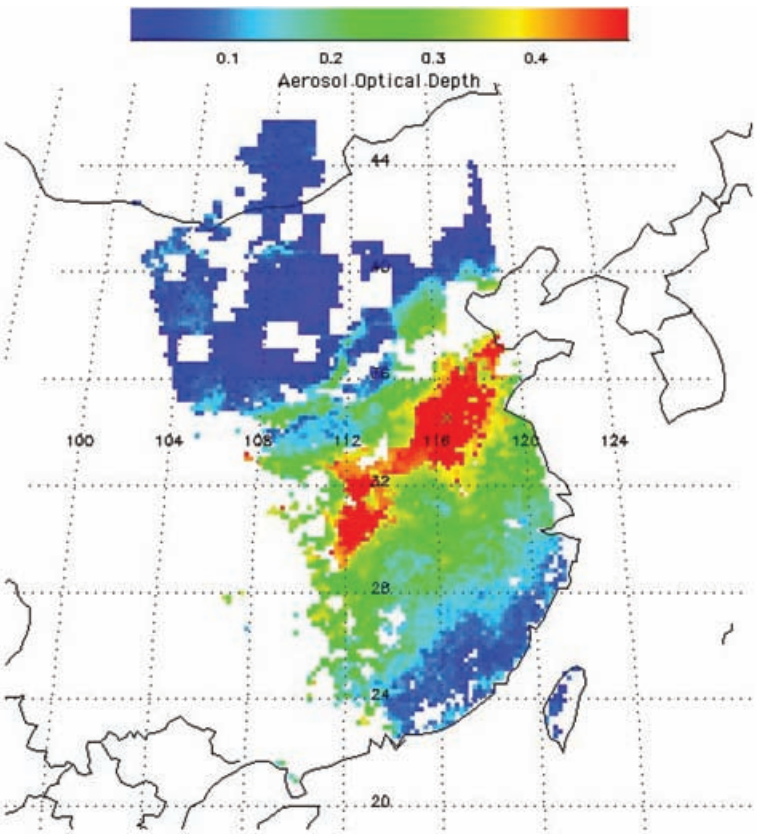

Fig. 10.6. Fine mode aerosol optical thickness retrieved at 865 nm by the PARASOL instrument over China (monthly average for February 2007).

different view angles. The fact that these fluctuations are not apparent in the residual errors demonstrates the effectiveness of Eqs. (18) and (19) for modeling the effects of surface polarized reflectance. The polarization generated by Fresnel reflection (i.e. R_p^f) progressively decreases with the scattering angle and becomes null in the backscattering direction ($\Theta = 180°$). Near backscattering the polarized reflectance is therefore determined by effects (multiple and internal scattering) that are not captured by a Fresnel model and that may also have some spectral dependence. It is therefore necessary to restrict the use of these simple Fresnel models to scattering angles smaller than 160° and indeed aerosol retrievals using polarized reflectances are only feasible with this limit on scattering geometries.

5. Aerosol retrievals using polarimetric observations

The use of polarized reflectance measurements for aerosol retrievals over land surfaces is substantially simpler and more robust than that using reflectance measurements because of the simpler lower boundary condition provided by the gray nature of the polarized reflectance of natural surfaces. The aerosol retrievals over land using polarized reflectance that have thus far been implemented for the POLDER and RSP instruments [Deuzé et al., 2001; Waquet et al., 2008] have therefore restricted themselves to using only polarized reflectance measurements, even though multi-angle reflectance measurements are also available, because reflectance measurements are more susceptible to cloud contamination and erroneous assumptions regarding the properties of surface reflectance. In this Section we describe two approaches to using polarized reflectances to retrieve aerosols over land.

5.1 The POLDER experience

The POLDER team pioneered the use of polarimetric measurements for aerosol retrievals over land surfaces. The principle of the algorithm currently used for the analysis of the PARASOL observations is based on the one developed for the POLDER instrument [Deuzé et al., 2001]. Improvements concerning the multiple scattering computations have been implemented in the present algorithm. The approach is to use a search of look-up tables (LUTs) to find the size and optical depth of aerosol that best fits the observations in two bands at 670 and 865 nm. The observations are simulated using a model based on Eqs (13) and (17) where the surface contribution is estimated based on its IGBP [Belward et al., 1999] classification and the current NDVI [Tucker, 1979]. The atmospheric contribution is calculated by interpolation within LUTs computed using a multiple scattering code. In order to account for the altitude of the pixel, the calculations are made for two values of molecular optical thickness corresponding to surface levels of 0 and 2 km. Calculations are made for several aerosol optical thicknesses varying between 0.0 and 2.0 at 865 nm and for 10 aerosol models. The aerosol polarization mainly comes from the small spherical particles [Vermeulen et al., 2000] whereas the coarse mode particles (e.g., mineral dust) do not polarize much [Herman et al., 2005] and therefore cannot be accurately detected with polarized measurements, at least in the spectral range between 670 and 865 nm. The aerosol models used in the algorithm consist of single lognormal size distributions of small spherical particles with effective radius varying between 0.075 and 0.225 μm and an effective variance of 0.175 (corresponding to the Ångström exponent varying between 3 and 1.8). Polarization measurements at 670 nm and 870 nm do not contain sufficient information to constrain the aerosol refractive index. As the method is mainly sensitive to fine mode particles, a refractive index of $1.47 - 0.01i$ is assumed for all retrievals, which is the mean value for urban-industrial and biomass burning aerosols [Dubovik et al., 2002]. As the majority of the anthropogenic particles have sizes that are within the fine mode, the POLDER missions allow one to locate the main sources of anthropogenic aerosols at a global scale. Fig. 10.6 shows the optical thickness due to small particles retrieved by PARASOL over China for February 2007.

The highest aerosol optical thicknesses appear in red on the images. We observe high optical thicknesses in the vicinity of Beijing with strong gradients across the China. Re-

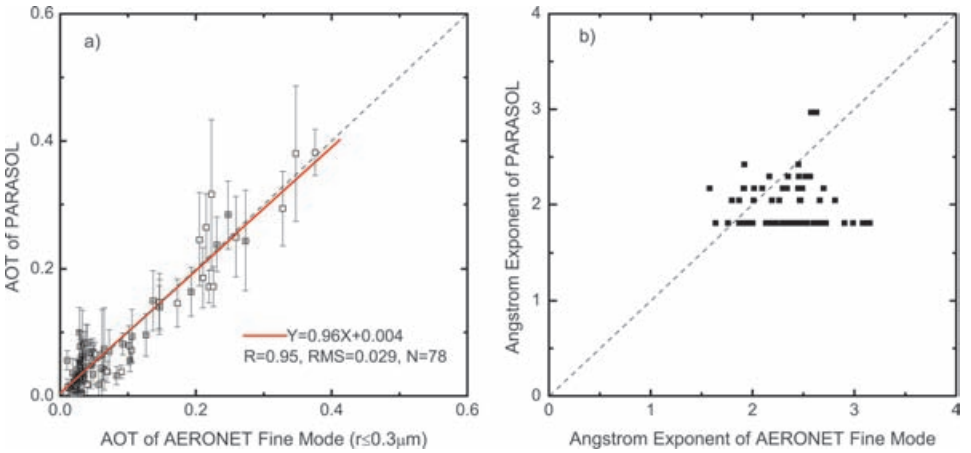

Fig. 10.7. PARASOL AOT and Ångström exponent versus those of AERONET for the fine mode fraction ($r_{eff} < 0.3$ μm) over Beijing.

gional validation performed over the northeast part of China has shown that the AOTs retrieved by PARASOL are consistent with the ones given by the federated Aerosol Robotic Network (AERONET) sunphotometers for the fine mode. The operational inversion algorithm developed for the analysis of the AERONET sunphotometer measurements provides the spectral aerosol optical thickness, the aerosol complex refractive index and the particle size distribution between 0.05 and 15 μm [Dubovik and King, 2000]. Fig. 10.7(a) shows a comparison between the PARASOL AOT and the ones given by AERONET for the fine mode ($r_{eff} < 0.3$ μm) for the city of Beijing [Fan et al., 2008]. A similar comparison of the Ångström exponent is shown in Fig. 10.7(b).

As shown in different studies [Chowdhary et al., 2005; Waquet et al., 2008] and discussed here after, polarization measurements at short visible wavelengths contain important information on the aerosol microphysical properties and the aerosol vertical extent. The PARASOL observations at 490 nm are well calibrated [Fougnie et al., 2007] and are also sensitive to the presence of mineral dust particles in the air [Fan et al., 2008] and to the altitude of the layer. Future efforts will therefore focus on the inclusion of the PARASOL band at 490 nm in the algorithm.

The use of a semi-empirical surface model and restricted spectral range (490–865 nm) limits the capacity of PARASOL to retrieve detailed aerosol microphysical properties over land [Deuze et al., 2001]. A multi-spectral airborne polarimeter has been recently developed by the Laboratoire d'Optique Atmosphérique and the French Centre National d'Etudes Spatiales. This instrument, called OSIRIS (Observing System Including PolaRisation in the Solar Infrared Spectrum), is based on the POLDER concept, but with the spectral range extended into the solar near-infrared spectrum with spectral bands at 1600 and 2100 nm. This instrument constitutes a crucial step in the development of a new European imaging polarimeter dedicated to the monitoring of the climate and air quality.

5.2 The RSP experience

The approach that is used for the analysis of the RSP observations [Waquet et al., 2008] and which is planned for use with the APS is an optimal estimation method. This approach is preferred to the use of a LUT because of the substantially higher information content of the seven RSP spectral bands that are located in atmospheric windows compared with the two spectral bands currently used in the POLDER approach. We therefore break this Section into two subsections: the theory of optimal estimation and our experimental implementation.

5.2.1 Theory

The principle of an optimal estimate is to determine the most probable atmospheric state conditional on the value of the measurements and some *a priori* knowledge of this medium and errors in measurement [Rodgers et al., 2000]. The determination of the most probable atmospheric state is identical to the minimization of a cost function Φ that accounts for these different quantities:

$$\Phi = (\mathbf{Y} - \mathbf{F})^T \mathbf{C}_T^{-1} (\mathbf{Y} - \mathbf{F}) + (\mathbf{X} - \mathbf{X}_a)^T \mathbf{C}_a^{-1} (\mathbf{X} - \mathbf{X}_a), \tag{20}$$

where $\mathbf{Y}$ is the measurement vector, $\mathbf{F}$ is the simulation vector, $\mathbf{C}_T^{-1}$ is the total error covariance matrix, $\mathbf{X}$ is the atmospheric state vector, $\mathbf{X}_a$ is the *a priori* atmospheric state vector and $\mathbf{C}_A^{-1}$ is the *a priori* error covariance matrix.

The first term in Eq. (20) corresponds to a weighted least squares error term that measures the distance between the observed polarized reflectances and the modeled polarized reflectances. We use the first six spectral bands of the RSP instrument that are in atmospheric windows (410, 470, 555, 670, 873 and 1590 nm) to constrain the aerosol properties. The observations are simulated using Eqs (18) and (19) and the polarized reflectance measured at 2250 nm is used to accurately model the surface. The residual atmospheric effect at 2250 nm is also accounted for in our retrieval process. We use the aerosol model retrieved with the shorter bands and a rearranged form of Eq. (18) to perform an atmospheric correction the polarized reflectance measured at 2250 nm.

The total error covariance matrix accounts for the measurement errors and some potential modeling errors. We assume that the different sources of errors are independent. Then, the total covariance matrix is given by the sum of the different error covariance matrices:

$$C_T = C_\varepsilon + C_{cal} + C_{pol} + \mathbf{C}_F. \tag{21}$$

The first term accounts for the effects of the instrumental noise, the second for uncertainty in the absolute calibration and the third one for the polarimetric accuracy. In the analysis presented here these error covariance matrices are filled out according to the signal, noise and accuracy obtained with the RSP instrument which is similar to that expected for the APS instrument (i.e. signal to noise ratio greater than 300 over dark oceans with typical aerosol loads, polarimetric accuracy for most scenes of 0.2 % or better and absolute radiometric accuracy of 5 %). $\mathbf{C}_F$ accounts for the effects of a change of the surface refractive index with wavelength and for the residual errors introduced by our modeling of the polarized reflectances (see Fig. 10.5).

Table 10.1. A priori knowledge of the aerosol parameters and associated uncertainties

	r_g, µm	σ	m_r	m_i
Fine mode	0.15 (0.1)	0.4 (0.1)	1.47 (0.14)	0.01 (0.015)
Coarse mode	0.8 (0.2)	0.6 (0.3)	1.53 (0.05)	0.005 (0.005)

The second term in Eq. (20) is a penalty function that constrains the solution to lie near the *a priori* state where the 'near' is quantified by the *a priori* error covariance matrix. The state vector $\mathbf{X}$ contains the aerosol parameters that allow characterizing each mode separately: N^f, r_g^f, σ^f, m_r^f, m_i^f, N^c, r_g^c, σ^c, m_r^c, m_i^c. The parameter N is the number density of aerosol particles (1/cm), r_g and σ are the parameters that define a lognormal size distribution (see Eq. (9) in Chapter 2 of this book), m_r and m_i are the real and imaginary refractive indices and the superscripts f and c denote the fine and coarse modes. We assume that aerosols are uniformly from the surface to a pressure level P, which is a reasonable assumption for a well-mixed boundary layer. The pressure level P should therefore correspond to the mixed layer depth. The *a priori* knowledge of the aerosol parameters is based on the aerosol climatology [Dubovik et al., 2002]. In Table 10.1, we provide the values of the *a priori* aerosol parameters (i.e. vector $\mathbf{X}_a$) and the associated uncertainties (standard deviation).

The covariance matrix $\mathbf{C}_a$ is assumed diagonal where the diagonal elements correspond to the square of the standard deviation values given in Table 10.1. The *a priori* values for N^f and N^c are derived using a LUT approach as explained in the following.

The determination of the best solution $\mathbf{X}$ that minimizes the cost function requires the resolution of a nonlinear equation. Nonlinear systems are usually solved using the Newton–Gauss iteration procedure. In practice, the Newton–Gauss procedure may not converge and needs to be modified. The most widely used modification is known as the Levenberg–Marquardt method, which is implemented by the following equation:

$$\mathbf{X}_{i+1} = \mathbf{X}_i - [\mathbf{H}(\mathbf{X}_i) + \gamma \cdot \mathbf{I}]^{-1} \cdot \nabla_x \Phi(\mathbf{X}_i), \tag{22}$$

where $\mathbf{I}$ is the identity matrix with the dimensionality of the state vector, i indicates the number of the iteration and γ is a positive coefficient that aids in the convergence of the iteration. $\mathbf{H}$ is known as the Hessian matrix,

$$\mathbf{H}(\mathbf{X}_i) = \nabla_X^2 \Phi(\mathbf{X}_i) \approx \mathbf{C}_a^{-1} + \mathbf{K}_i^T \cdot \mathbf{C}_T^{-1} \cdot \mathbf{K}_i \tag{23}$$

where

$$\mathbf{K}_i = \frac{\partial \mathbf{F}(\mathbf{X})}{\partial \mathbf{X}_i}. \tag{24}$$

$\mathbf{K}$ is the Jacobian matrix, which represents the sensitivity of the forward model to the retrieved quantity (i.e. sensitivity of the polarized reflectances to the aerosol parameters).

The criteria for changing the γ value is dependent on the convergence behavior. If $\Phi(\mathbf{X}_{i+1}) > \Phi(\mathbf{X}_i)$ then we reject the solution $\mathbf{X}_{i+1}$ and we increase γ whereas if $\Phi(\mathbf{X}_{i+1}) < \Phi(\mathbf{X}_i)$ then we accept the solution $\mathbf{X}_{i+1}$ and we decrease γ. For larger γ values the steepest descent dominates and the convergence is slow (i.e. small step size) but robust whereas for smaller γ values, the search turns to the faster Newtonian descent. The ite-

ration process is stopped when there is no change of the cost function between two successive iteration steps.

The optimal estimate method also provides an error diagnostic of the retrieved parameters. The Hessian matrix obtained at the final step of iteration can be used to calculate the retrieval error covariance matrix $\mathbf{C}_x$:

$$\mathbf{C}_x = \left(\mathbf{C}_a^{-1} + \mathbf{K}_i^T \cdot \mathbf{C}_T^{-1} \cdot \mathbf{K}_i\right)^{-1}. \tag{25}$$

The square roots of the diagonal elements of $\mathbf{C}_x$ give the standard deviation associated with each retrieved parameter. The aerosol microphysical parameters contained in the vector $\mathbf{X}$ and the error retrieval covariance matrix $\mathbf{C}_x$ can also be used to calculate the standard deviation, or retrieval uncertainty, associated with the optical aerosol parameters. For the aerosol optical thickness, the standard deviation is given by:

$$\sigma_\tau = \sqrt{\left(\sum_{i=1}^{N}\sum_{j=1}^{N} C_{x,i,j}\frac{\partial\tau}{\partial X_i}\frac{\partial\tau}{\partial X_j}\right)}. \tag{26}$$

A similar formula applies for the single scattering albedo ϖ_0.

A first guess of the aerosol parameters $(\mathbf{X}_0)$ is required to start the iterative process. A good first guess allows the number of iterations to be reduced and alleviates the problem of finding a solution $\mathbf{X}$ that is only a local minimum of the cost function Φ. A LUT provides a simple and effective approach to derive a first estimate of the aerosol optical thickness and aerosol model. In the LUT used for aerosols retrievals over land the polarized reflectances are calculated for various aerosol optical thicknesses and aerosol models. Twelve fine mode models are considered ($r_g^f = 0.05,\ 0.1,\ 0.15,\ 0.2$ µm, $\sigma_f = 0.4$, $m_r = 1.4,\ 1.47,\ 1.54$, $m_i = 0.01$). We also include the coarse mode particle model described in Table 10.1. The polarized reflectances are calculated for aerosol optical thicknesses at a reference wavelength of 550 nm equal to 0, 0.05, 0.1, 0.2, 0.4, 0.8, 1 and 2 and an interpolation process is used to create a fine step. The first guess corresponds to the aerosol model and aerosol optical thickness that minimize the least squares error term (see Eq. (20)) calculated between the measurements and the simulations. The properties of the coarse mode particles are not given the same level of detail in the LUT because the sensitivity of polarized reflectance measurements to coarse mode particles is limited by their weak spectral variation (similar to the surface) and weak polarization signal. As a first guess, the aerosol optical thickness of the coarse mode (at 550 nm) is assumed to be a tenth of the total aerosol optical thickness. The properties of the aerosol models considered in the LUT allow the number density of particles associated with each mode to be derived. In retrievals the LUT is assumed to reduce the uncertainties in r_g^f and m_r^f given in Table 10.1 to 0.05 and 0.07, respectively, and we assume that the relative uncertainty for both N^f and N^c is 100 %.

The residual atmospheric effect is accounted for in the retrieval process. This effect is usually small and mainly depends on the aerosol size and load [Waquet et al., 2007]. The aerosol model retrieved with the shorter bands is used in a rearranged form of Eq. (17) to perform an atmospheric correction on the polarized reflectance measured at 2250 nm. This correction is performed before the first iteration using the retrieved parameters obtained

with the LUT approach and is refined after each iteration step. The final results from the retrieval are the estimate of the state vector **X** that describes the aerosol model and the uncertainty in that state vector calculated using Eq. (25).

The information contained in polarization measurements is mainly dominated by the single scattering properties of the aerosol. The angular dependence of the single scattering of polarized light is given by the polarized phase function (P_{12} element of the aerosol scattering phase matrix), which is a particular function of the scattering angle. The variations of the polarized phase function with the scattering angle and wavelength are strongly dependent on the aerosol microphysical properties [Mishchenko et al., 2006]. Fig. 10.8 illustrates the sensitivity of the observed polarized reflectance to various aerosol parameters as a function of the wavelength and scattering angle.

We note the large angular and spectral dependences of the polarized reflectance on the particle size and on the real part of the refractive index. Fig. 10.8 also shows that polarization measurements in the shortest visible bands are sensitive to the aerosol absorption (i.e. imaginary part of the complex refractive index) and to the height that they are mixed to (i.e. the mixed layer depth, P). The sensitivity to these latter parameters mainly appears in the UV and blue part of the spectrum where the molecular and multiple scattering contributions are significant.

The retrieval error covariance matrix defined in Eq. (25) can be used to simulate the retrieval errors obtained for any instrument type and surface–atmosphere system with synthetic measurements. Fig. 10.9 shows an example of retrieval errors obtained for $\tau(\lambda)$, $v_0(\lambda)$, $m_r\lambda)$, r_{eff}, v_{eff} of each mode and pressure as a function of the aerosol optical thickness at 550 nm. Calculations are made for an aerosol model representative of pollutant particles following Dubovik et al. [2002]. The error covariance matrix is modeled accord-

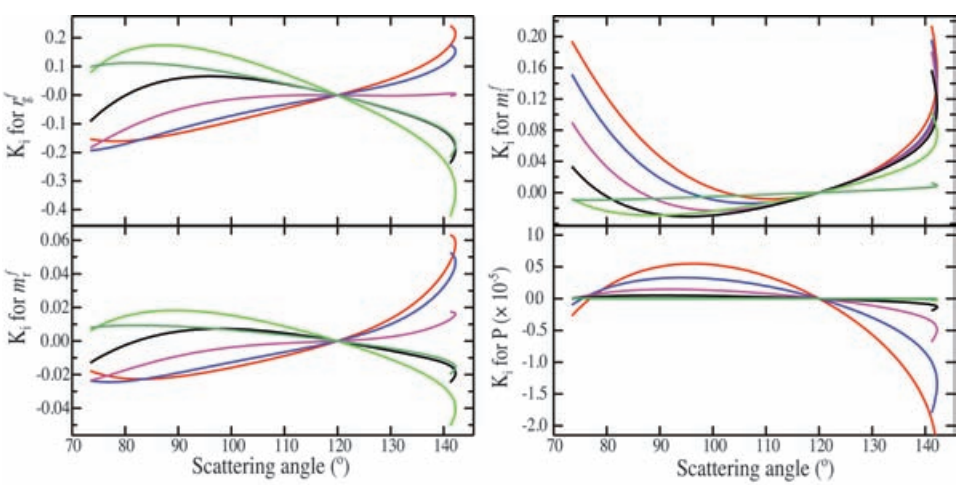

Fig. 10.8. Elements of the Jacobian matrix calculated for m_r^f, m_i^f, r_g^f and P as a function of the scattering angle and wavelength. Polarized reflectance calculated for an aerosol model described by a single log-normal size distribution ($r_g = 0.1$, $\sigma = 0.403$) and a complex refractive index of 1.44-0.01i. Calculations performed for $\theta_s = 60°$ and $\Delta\varphi = 45°$ and an aerosol optical thickness of 0.5 at 550 nm and including a surface polarized reflectance. The wavelengths are: 0.41, 0.47, 0.55, 0.67, 0.865 and 1.6 μm, respectively in red, blue, magenta, black, green and dark green.

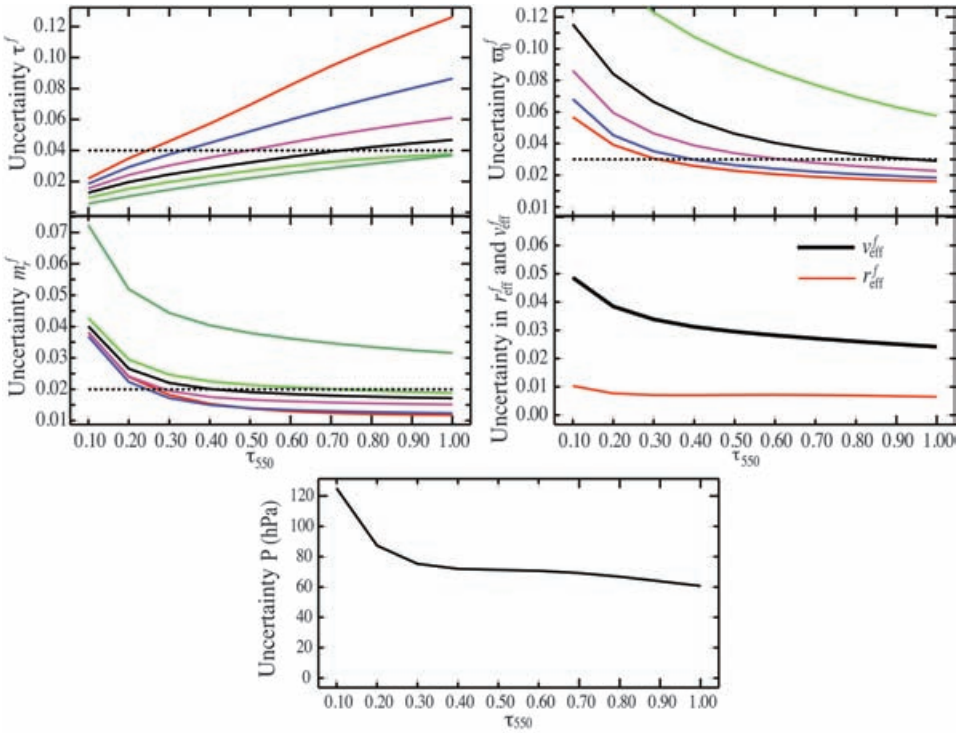

Fig. 10.9. Retrieval errors (see Eq. (26)) of the spectral aerosol optical thickness (a), single scattering albedo (b), real part of the refractive index (c), effective radius and effective variance (d) and pressure of the top of the aerosol layer as a function of the aerosol optical thickness at 550 nm. The dashed lines correspond to the absolute accuracy requirements suggested by Mishchenko et al. [2004]. Computations are performed at TOA for $\theta_s = 45°$ and $\Delta\varphi = 45°$. The wavelengths are 410, 470, 555, 670, 865 and 1600 nm, respectively in red, blue, magenta, black, green and dark green.

ing to the instrumental characteristics of the RSP instrument and the *a priori* information given in Table 10.1.

Mishchenko et al. [2004] suggested the following retrieval requirements for climate research over land: 0.04 or (10 %) for the aerosol optical thickness, 0.03 for the single scattering albedo, 0.1 micron (or 10 %) for the effective radius, 0.3 (or 50 %) for the effective variance, and 0.02 for the real part of the refractive index. This sensitivity analysis shows that the uncertainties in aerosol optical thickness (AOT) increase with AOT while the uncertainties in the microphysical model decrease. The uncertainty in the single scattering albedo (SSA) is notably less than 0.05 by the time the AOT is greater than 0.2. The increase in the errors associated with the AOT is explained by the fact that the errors in the column number density of particles N increase with N (not shown) and because the AOT is closely connected to this parameter. The relative retrieval errors in the AOT, however, decrease for increasing AOT and remain under the required value for all the wavelengths considered here ($\sigma_\tau(\lambda)/\tau(\lambda) < 10\,\%$). The requirements for r_{eff} and v_{eff} are reached for any AOT values larger than 0.1 at 550 nm, whereas for m_r and v_0, the requirements are only reached in three spectral bands (410, 470 and 550 nm) and for AOT respectively larger than

0.3 and 0.6. Figure 10.9 shows that there is also useful information about the height of the top of the aerosol layer. The error in the pressure level of the top of the aerosol layer is less than 70 hPa for AOT greater than 0.6 at 550 nm when the true mixed layer depth is $P = 700$ hPa. This corresponds to an error of 0.8 km when the aerosol altitude is 3 km. It is important to note that we are primarily interested in retrieving P to ensure that large retrieval and/or fitting errors do not occur in the presence of thick aerosol layers such as smoke plumes and that erroneous assumptions about P do not therefore cause a bias in our retrievals. This aerosol layer pressure top estimate is based on the fact that aerosols reduce the polarized reflectance at 410 and 470 nm. This happens because the aerosols attenuate molecular scattering below the aerosol layer, while their own polarized reflectance contribution is less than that from molecular scattering, even for very small particles.

5.2.2 Experiment

We applied the method described above to a set of field experiment observations performed with the RSP that provide a test of the realism of the analysis for various aerosol optical depth regimes. Figure 10.10 shows three examples of scans of polarized reflectance acquired during the Aerosol Lidar Validation Experiment (ALIVE) and the Megacity Initiative: Local And Global Research Observations (MILAGRO) field campaign. The ALIVE experiment took place over the Department of Energy Atmospheric Radiation Measurements [Ackerman and Stokes, 2003] program facility in the Southern Great Plains (SGP). The RSP instrument participated in this campaign onboard the Sky Research Inc. Jetstream-31 (J31) research aircraft and acquired data throughout all twelve flights performed between September 12 and 22, 2005. The MILAGRO experiment was an international, multi-agency campaign involving numerous academic and research institutions from the USA, Mexico and other countries [Fast et al., 2007]. This campaign was designed to study pollution from Mexico City and regional biomass burning (sources, transport, transformations and effects) and involved intensive aircraft and ground-based measurements. The RSP instrument flew onboard the J31 between March 3 and 20, 2006, and participated in 13 flights. A variety of aerosol, cloud, water vapor, and surface conditions were sampled over Mexico City and the Gulf of Mexico. During these two campaigns the NASA Ames Airborne Tracking 14-Channel Sun-photometer (AATS-14) was also integrated onto the J31. These measurements allowed the aerosol optical thickness of the column above the aircraft to be derived in 13 bands between 353 and 2105 nm [Schmid et al., 1997; Russell et al., 1999]. A cloud-screening algorithm has been developed for the analysis of the AATS measurements and allowed us to select scenes for which the direct beam of the sun was cloud-free above the aircraft that eliminated concerns regarding cirrus clouds.

In Table 10.2 we summarize the observational and illumination geometry of the three example scenes presented here. Panels (a) and (b) in Fig. 10.10 show scans performed on September 16 and 19, 2005, during the ALIVE experiment, close to the AERONET station denoted to be CART (N36.6069°, W97.4858°). The spikes in these scans, that are correlated across all spectral bands and that are present particularly in Fig. 10.10(a), are the result of different view angles seeing different surface types, since the data have not been reorganized to view the same point on the ground. During the ALIVE experiment,

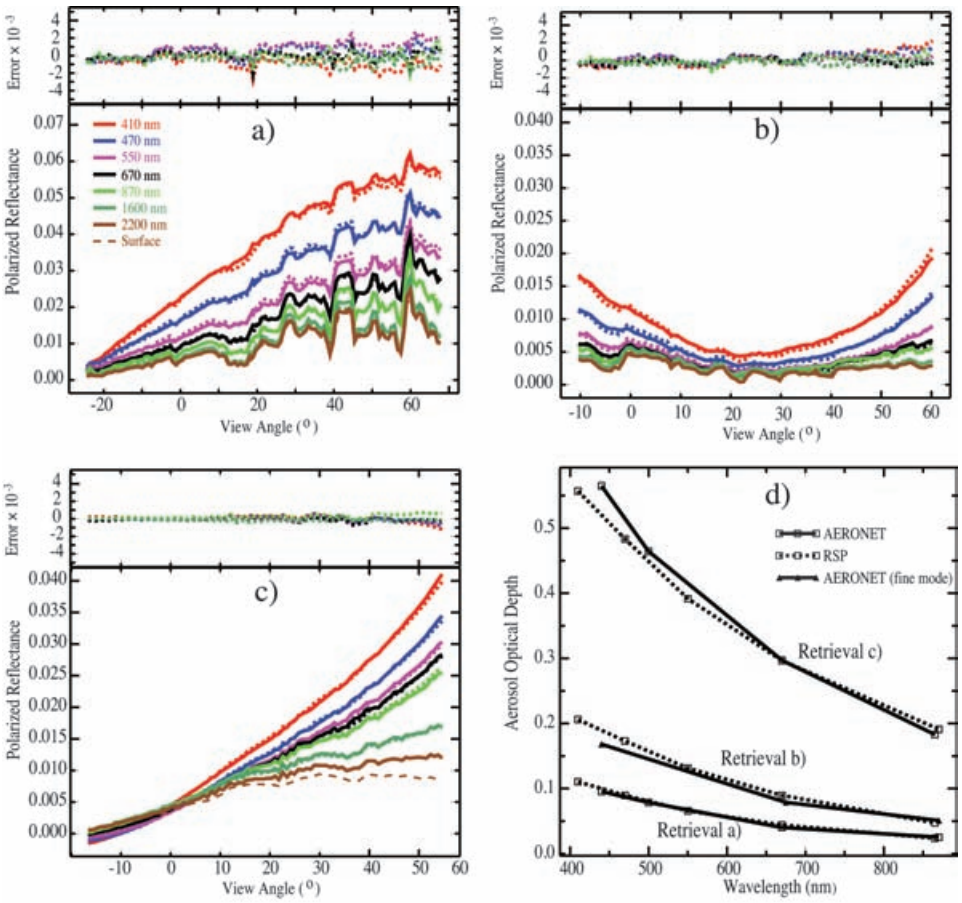

Fig. 10.10. (a), (b), (c) Polarized reflectance measured at the aircraft level (solid lines) and simulated polarized reflectance (dashed lines) as a function of the viewing angle. The wavelengths are 410, 470, 555, 670, 865, 1600 and 2250 nm, respectively in red, blue, magenta, black, green, dark green and brown. The dashed brown line corresponds to the direct surface contribution (measurements at 2250 nm corrected from the atmospheric effects). The error is the difference between the simulated and measured polarized reflectances and is shown at the top of the figures. Scans (a) and b) were obtained on 09/16/05 and 09/19/05 during the ALIVE experiment (Southern Great Plains, USA). Scan (c) was obtained over Mexico City on 03/15/06 during the MILAGRO experiment. (d) Aerosol optical thicknesses retrieved by the RSP instrument from the measurements shown in (a), (b) and (c) and coincident AERONET measurements (or retrievals when the fine mode AOT is reported) as a function of the wavelength.

the flights were performed for low aerosol loading ($\tau < 0.165$ at 500 nm) and we therefore did not try to retrieve the absorption and the altitude of the aerosol since the sensitivity to these parameters is weak at such low AOT. The two scans shown here were performed in different planes of observation, which provided measurements with different ranges of scattering angle. We observe that the use of the 2250 nm measurement in Eqs. (18) and (19) allows the effects of the various surface types to be compensated extremely effectively. The coarse-mode AOT is negligible for the scan shown in Fig. 10.10(a) and

Table 10.2. Illumination and viewing geometry of the three datasets presented in Fig. 10.10.

Scan	Viewing geometry		
	Scattering angle, deg	Solar zenith angle, deg	The difference of azimuths, deg
a	70–160	56.0	– 186
b	135–160	36.5	37
c	85–170	24.1	– 175

reaches 0.05 at 670 nm for Fig. 10.10(b). Figure 10.10(d) shows a comparison between the AOT retrieved by the RSP and those measured by AERONET. These results show that our approach allows the AOT of the fine mode particles to be retrieved with a maximal error of 0.01 for an AOT of 0.08 at 670 nm. The spectral dependence of the AOT estimate agrees well with the sunphotometer measurements, which suggests that the microphysical properties of the observed aerosol (i.e. the particle size and the real part of the refractive index), are also correctly estimated. This conclusion is born out by the agreement of the RSP inversion of the data shown in Fig. 10.10(b) with an inversion of AERONET sun-photometer measurements that was made close to the time of the RSP observations. The difference between the effective radii and refractive index retrievals from these two data sets is 0.025 μm and 0.003 respectively. This comparison also indicated that there is little sensitivity of the polarized reflectance observations to the coarse particle mode at least for coarse-mode AOTs less than 0.05 with a very large coarse particle mode.

Figure 10.10(c) shows a scan acquired on March 15, 2006, around 1800 UT during the MILAGRO experiment over the ground-based site called T0. This site was located in the urban area of Mexico City and was equipped with an AERONET sunphotometer (N19.4900°, W99.1478°). For this scan, the data are reorganized so that each part of the scan sees the same target at the ground, as is the case for observations taken from satellites. It is also interesting to notice that the residual atmospheric effect at 2250 nm is not negligible for this case and must be taken into account (see the differences between the solid and dashed brown lines in Fig. 10.10(c)). The contribution of the coarse-mode particles to the total AOT is quite stable during the day and has an average value of 0.02 at 550 nm.

The retrieved AOT is equal to 0.3 (0.005) at 670 nm, the effective radius and the effective variance are respectively equal to 0.15 (0.005) μm and 0.485 (0.01), the real and imaginary refractive indices are equal to 1.54 (0.01) and 0.027 (0.005), respectively and P is equal to 627 hPa (10), corresponding to a height of about 3.85 km. The parenthetic values are the uncertainties in the retrievals calculated using Eq. (26). We retrieve a small effective radius and a high real refractive index, which is characteristic of the properties of the biomass burning particles [Dubovik et al., 2002]. The retrieved imaginary refractive index leads to a single scattering albedo of 0.865 (0.005) at 550 nm. This value is similar to estimates made for African savanna biomass burning particles ($0.84 < \omega_0 < 0.88$) and for fresh biomass burning particles observed in the vicinity of the source (0.86) [Schmid et al., 2003]. Figure 10.10(d) shows that the AOT retrieved by the RSP is in good agreement with the coincident AOT measured by AERONET over a large spectral range, which indicates that our retrieved aerosol model is valid. An inversion of the AERONET sunphotometer measurements was made at the T0 site earlier in the afternoon (15:25 UT). However the

Ångström exponent measured by AERONET is equal to 1.65 at 15:25 UT when this inversion was performed but changes to 1.9 by 18:00 UT close to the time that the RSP observations were made. This indicates that the fine mode particles observed at 15:25 UT were different to those observed at 18:00 UT. A comparison of the RSP and AERONET microphysical retrievals is therefore not useful in this case. Analysis of the chemical composition of the aerosols observed at the T0 site was made for the period March 15–27, 2006 [Moffett et al., 2008]. It was found that biomass burning and aged organic carbon particle types respectively constituted 40 % and 31 % of the submicrometer mode on average and that the fresh biomass fraction dominated in the afternoons (around 65 % at the time of the RSP observations). This composition is the result of many fires to the south and southeast of the city on the surrounding mountains and the local meteorological conditions and is coherent with the RSP microphysical retrieval showing quite strongly absorbing aerosols. The NASA Langley Research Center High Spectral Resolution Lidar (HSRL) [Hair et al., 2008] flew over the T0 site an hour prior the RSP overpass. This instrument measures, among other things, the aerosol backscattering coefficient at 532 nm. The HSRL measurements show that the aerosols were located between the ground and 3.4 km, which indicates that our estimate of the aerosol top layer height is also realistic.

6. Conclusions

It has become apparent over the last few years, based on the measurements presented here as well as previous work that the surface polarized reflectance is indeed almost perfectly gray (less than 0.001 variation in the polarized reflectance) over the entire solar and shortwave infrared spectrum from 400 to 2,300 nm. This is of particular importance given the apparently similar spectral invariance of the angular shape of the surface reflectance and the consequent correlation between reflectance shape properties and the surface polarized reflectance [Elias et al., 2004]. We have hitherto not used the reflectance measurements over land for aerosol retrievals from POLDER, or RSP, because of a tendency to degrade the quality of the retrievals obtained using only polarized reflectances. However, based on the results presented in this book, it would appear that careful use of the spectral invariance of the angular shape of the surface reflectance in conjunction with the spectral invariance of the polarized reflectance would provide even stronger constraints on the aerosol retrievals than the current approaches used for analysis of POLDER and RSP data. This extension of the retrieval approach using polarized reflectances presented here to incorporate the techniques used for multi-angle reflectance measurements presented elsewhere in this book is an area of ongoing research.

The POLDER retrieval algorithms have proven themselves to be robust and globally applicable with particular sensitivity to the fine mode particles that are primarily of anthropogenic origin in many areas and excellent coherence between retrievals over ocean and land. The addition of the shorter wavelength band at 490 nm is expected to improve detection of dust aerosols that are currently difficult to identify using just two bands at 670 and 865 nm. The RSP retrieval algorithms are more computationally intensive than those used for POLDER, but do have the advantage that the addition of other measurements sources (such as the multi-angle reflectance measurements) are fairly straightforward and assump-

tions regarding sizes and composition (refractive indices) are minimized. A retrieval approach of this kind is in fact necessary for the analysis of RSP data because of the larger number of spectral bands (seven as compared to three) and viewing angles (152 as compared to 12) and the need to appropriately weight the information in each measurement. In addition a major advantage of optimal estimation methods is the provision of uncertainties with the retrieval products [Rodgers, 2000] so that appropriate statistical weighting can be used when estimating mean values and their uncertainties. Having retrieval uncertainties available is particularly helpful when one is interested in something that is derived from the retrieval products. One example of this is the absorption AOT which is the product of the AOT and the single scattering co-albedo (i.e. $(1 - \nu)\tau$). The uncertainty in this quantity and not the uncertainty in the single scattering albedo is what is really important in estimating the effect of absorption by aerosols. If one examines the uncertainty in this quantity as a function of AOT using Figure 10.9 it is apparent that the absorption AOT can be retrieved to better than for an AOT of 0.2 and that the uncertainty in its retrieval increases to almost 0.03 at an AOT of 0.8. The RSP retrievals of absorption AOT are therefore useful at all optical depths, even though the single scattering albedo is highly uncertain at low optical depths. In summary, the sensitivity analyses and results presented here show that passive polarimetric remote sensing has an excellent capability to determine the size, composition, amount and useful vertical distribution information for aerosols over land.

Acknowledgments. Figure 10.7 was prepared by X. Fan from the Institute of Atmospheric Physics of the Chinese Academy of Sciences and we would like to express our thanks to him for providing this to us. We would also like to thank the personnel from NASA Ames Research Center led by P.B. Russell, B. Schmid (now at PNNL, Richmond, Washington, USA) and J. Redemann for facilitating the participation of the RSP instrument in the ALIVE and MILAGRO field experiments. The work described here has been carried out at NASA Goddard Institute for Space Studies and the Laboratoire d'Optique Atmosphérique of the University of Lille. Support of the NASA Radiation Sciences Program managed by H. Maring and the NASA Glory project is gratefully acknowledged. Finally we would like to thank M. Mishchenko, L. Travis, R.A. Chandos and E. Russell for assistance in the acquisition of the data used here and in the preparation of this paper.

References

Ackerman, T.P., and G.M. Stokes, 2003: The atmospheric radiation measurement program, *Physics Today*, **56**, DOI:10.1063/1.1554135.

Babinet, J., 1840: Sur un nouveau point neutre dans l'atmosphere, *C. R. Acad. Sci. Paris*, **11**, 618–620.

Barral, M.J.A., 1858: *Oeuvres de Francois Arago I–V*, Gide, Paris.

Belward, A.S., J.E. Estes, K.D. Kline, 1999: The IGBP-DIS global 1-km land-cover data set discover: A project overview, *Photogramm. Eng. Rem. Sensing*, **65**, 1013–1020.

Bréon, F.M., D. Tanré, P. Leconte, and M. Herman, 1995: Polarized reflectance of bare soils and vegetation: measurements and models, *IEEE Trans. Geosci. Remote Sens.*, **33**, 487–499.

Brewster, D., 1842: On the existence of a new neutral point and two secondary neutral points, *Rep. Brit.-Assoc. Adv. Sci.*, **2**, 13–25.

Cairns, B., L.D. Travis, and E.E. Russell, 1999: The Research Scanning Polarimeter: calibration and ground-based measurements, *Proc. SPIE*, **3754**, 186–197.

Chipman, R.A., 1994: Polarimetry, in *Handbook of Optics: Devices, Measurements and Properties*, 2nd edn. M. Bass (Ed.), McGraw-Hill, New York, Vol. II, pp. 1–37.

Chowdhary, J. et al., 2005: Retrieval of aerosol scattering and absorption properties from photo-polarimetric observations over the ocean during the CLAMS experiment, *J. Atmos. Sci.*, **62**, 1093–1117, doi:10.1175/JAS3389.1.

Coulson, K.L., 1988: *Polarization and Intensity of Light in the Atmosphere, A Deepak, Hampton, VA.*

d'Almeida, G.A., P. Koepke, and E.P. Shettle, 1991: *Atmospheric Aerosols, Global Climatology and Radiative Characteristics*, A. Deepak, Hampton, VA.

Deschamps et al., 1994: The POLDER mission: instrument characteristics and scientific objectives, *IEEE Trans. Geosci. Remote Sens.*, **32**, 598–615.

Deuzé, J.-L. et al., 2001: Remote sensing of aerosols over land surfaces from POLDER-ADEOS-1 polarized measurements, *J. Geophys. Res.*, **106**, 4913–4926.

Diner, D. J. et al., 2007: Dual-photoelastic-modulator-based polarimetric imaging concept for aerosol remote sensing, *Appl. Opt.*, **46**, 8428–8440.

Dubovik, O., and M. D. King, 2000: A flexible inversion algorithm for retrieval of aerosol optical properties from Sun and sky radiance measurements, *J. Geophys. Res.*, **105**, 20673–20696.

Dubovik, O. et al., 2002: Variability of absorption and optical properties of key aerosol types observed in worldwide locations, *J. Atmos. Sci.*, **59**, 590–608.

Elias, T., B. Cairns, and J. Chowdhary J., 2004: Surface optical properties measured by the airborne research scanning polarimeter during the CLAMS experiment, in *Remote Sensing of Clouds and the Atmosphere VIII*, K.P. Schäfer, A. Cameron, M.R. Carleer, R.H. Picard (Eds), *Proc. SPIE, 5235*(#79), SPIE, Bellingham, WA, pp. 595-606.

Fan, X., P. Goloub, J.-L. Deuzé, H. Chen, W. Zhang, D. Tanré, and Z. Li, 2008: Evaluation of PARASOL aerosol retrieval over North East Asia, *Rem. Sens. Env.*, **112**, 697–707.

Fast, J.D. et al., 2007: A meteorological overview of the MILAGRO field campaigns, *Atmos. Chem. Phys.*, **7**, 2233–2257.

Hair, J.W. et al., 2008: Airbonc High Spectral Resolution Lidar for profiling aerosol optical properties, *Appl. Opt.*, **47**, 6734–6752, doi:10.1364/AO.47.006734.

Fougnie, B., G. Bracco, B. Lafrance, C. Ruffel, O. Hagolle, and C. Tinel, 2007: PARASOL in-flight calibration and performance, *Appl. Opt.*, **46**, 5435–5451.

Grant, L., C.S.T. Daughtry, and V.C. Vanderbilt, 1993: Polarized and specular reflectance variation with leaf surface features, *Physiologia Plantarum*, **88**, 1–9.

Hagolle, O. et al., 1999: Results of POLDER in-flight calibration, *IEEE Trans. Geosci. Remote Sens.*, **37**, 1550–1566.

Hansen, J.E., and L.D. Travis, 1974: Light scattering in planetary atmospheres, *Space Sci. Rev.*, **16**, 527–610.

Hasekamp, O.P., and J. Landgraf, 2007: Retrieval of aerosol properties over land surfaces: capabilities of multiple-viewing-angle intensity and polarization measurements, *Appl. Opt.*, **46**, 3332–3344, doi:10.1364/AO.46.003332.

Herman, M., et al., 2005: Aerosol remote sensing from POLDER/ADEOS over the ocean: improved retrieval using a nonspherical particle model, *J. Geophys. Res.*, **110**, D10S02, doi:10.1029/2004JD004798.

Holben, B., et al., 1998: AERONET – a federated instrument network and data archive for aerosol characterization. *Rem. Sens. Environ.*, **66**, 1–16.

Jones, S., F. Iannarilli, and P. Kebabian, 2004: Realization of quantitative-grade fieldable snapshot imaging spectropolarimeter, *Opt. Express*, **12**, 6559–6573.

Kaufman, Y.J. et al., 1997: Remote sensing of tropospheric aerosol from EOS-MODIS over the land using dark targets and dynamic aerosol models. *J. Geophys. Res.*, **102**, 17051–17067.

Kawata, Y., 1978: Circular polarization of sunlight reflected by planetary atmospheres, *Icarus*, **33**, 217–232.

Keller, C.U., 2002: Instrumentation for astrophysical spectropolarimetry, in *Astrophysical Spectropolarimetry*, J. Trujillo-Bueno, F. Moreno-Insertis, and F. Sánchez (Eds), Cambridge University Press, Cambridge, UK, pp. 303–354.

Lafrance, B., 1997: Modélisation simplifiée de la lumière polarisée émergeant de l'atmosphère. Correction de l'impact des aérosols stratosphériques sur les mesures de POLDER. Thèse, Université des Sciences et Techniques de Lille. Lebsock, M.D., T.S. L'Ecuyer, and G.L. Stephens, 2007: Information content of near-infrared spaceborne multiangular polarization measurements for aerosol retrieval, *J. Geophys. Res.*, **112**, doi:10.1029/2007JD008535.

Mishchenko, M.I., B. Cairns, J.E. Hansen, L.D. Travis, R. Burg, Y.J. Kaufman, J.V. Martins, and E.P. Shettle 2004. Monitoring of aerosol forcing of climate from space: analysis of measurement requirements. *J. Quant. Spectrosc. Radiat. Transfer* **88**, 149–161, doi:10.1016/j.jqsrt.2004.03.030.

Mishchenko, M.I., L.D. Travis, and A.A. Lacis, 2006: *Multiple Scattering of Light by Particles: Radiative Transfer and Coherent Backscattering*, Cambridge University Press, Cambridge, UK.

Mishchenko, M.I., B. Cairns, G. Kopp, C.F. Schueler, B.A. Fafaul, J.E. Hansen, R.J. Hooker, T. Itchkawich, H.B. Maring, and L.D. Travis, 2007: Precise and accurate monitoring of terrestrial aerosols and total solar irradiance: introducing the Glory mission. *Bull. Amer. Meteorol. Soc.*, **88**, 677–691, doi:10.1175/BAMS-88-5-677.

Moffet, R.C., B. de Foy, L.T. Molina, M.J. Molina, and K.A. Prather, 2008: Measurement of ambient aerosols in northern Mexico City by single particle mass spectrometry, *Atmos. Chem. Phys.*, **8**, 4499–4516.

Nadal, F., and F.M. Bréon, 1999: Parameterization of surface polarized reflectances derived from POLDER spaceborne measurements, *IEEE Trans. Geosci. Remote Sens.*, **37**, 1709–1719.

Oka, K., and T. Kato, 1999: Spectroscopic polarimetry with a channeled spectrum, *Opt. Lett.*, **24**, 1475–1477.

Pollack, J.B., O.B. Toon, and B.N. Khare, 1973: Surface refractive index, *Icarus*, **19**, 372–389.

Povel, H., H. Aebersold, and J.O. Stenflo, 1990: Charge-coupled device image sensor as a demodulator in a 2-D polarimeter with a piezoelastic modulator, *Appl. Opt.*, **29**, 1186–1190.

Raman, C.V., 1921: A method of improving the visibility of distant objects, *Nature* (London) **108**, 242.

Redemann, J., Q. Zhang, B. Schmid, P.B. Russell, J.M. Livingston, H. Jonsson, and L.A. Remer, 2006: Assessment of MODIS-derived visible and near-IR aerosol optical properties and their spatial variability in the presence of mineral dust, *Geophys. Res. Lett.*, **33**, L18814, doi:10.1029/2006GL026626.

Rodgers C.D., 2000: *Inverse Methods for Atmospheric Sounding, World Scientific.*

Rondeaux, G., and M. Herman, 1991: Polarization of light reflected by crop canopies. *Rem. Sens. Environ.*, **38**, 63–75.

Russell, P.B., J.M. Livingston, P. Hignett, S. Kinne, J. Wong, A. Chien, R. Bergstrom, P. Durkee, and P.V. Hobbs (1999), Aerosol-induced radiative flux changes off the United States mid-Atlantic coast: comparison of values calculated from sunphotometer and in situ data with those measured by airborne pyranometer, *J. Geophys. Res.*, **104**(D2), 2289–2307.

Schmid, B., et al., 1997: Retrieval of optical depth and particle size distributions of tropospheric and stratospheric aerosols by means of sun photometry, *IEEE Trans. Geosci. Remote Sens.*, **35**, 172–181.

Schmid, B. et al., 2003: Column closure studies of lower tropospheric aerosol and water vapor during ACE-Asia using airborne Sun photometer and airborne in situ and ship-based lidar measurements, *J. Geophys. Res.*, **108**(D23), 8656, doi:10.1029/2002JD003361.

Shettle, E.P., and R.W. Fenn, 1979: Models for the aerosols of the lower atmosphere and the effect of humidity variations on their optical properties, Tech. Rep., AFGL-TR-79-0214, Air Force Geophys. Lab., Hanscomb AFB, MA.

Strutt, J.W. (Lord Rayleigh), 1871: On the light from the sky it polarization and color, *Phil. Mag.* **XLI**, 107–120. Reprinted in *Scientific Papers*, Vol. I, Cambridge University Press, Cambridge, UK, 1899.

Torres, O., P.K. Bhartia, J.R. Herman, Z. Ahmad, and J. Gleason (1998), Derivation of aerosol properties from satellite measurements of backscattered ultraviolet radiation: theoretical basis, *J. Geophys. Res.*, **103**(D14), 17099–17110.

Tucker, C.J., 1979: Red and photographic infrared linear combination for monitoring vegetation. *Rem. Sens. Environ.* **8**, 127–150.

Vanderbilt V.C. et al., 1985: Specular, diffuse, and polarized light scattered by two wheat canopies, *Appl. Opt.*, **24**, 2408–2418.

Vermeulen, A., C. Devaux, and M. Herman, 2000: Retrieval of the scattering and microphysical properties of aerosols from ground-based optical measurements including polarization. I. Method, *Appl. Opt.*, **39**, 6207–6220.

Waquet F., P. Goloub, J.-L. Deuzé, J.-F. Léon, F. Auriol, C. Verwaerde, J.-Y. Balois, and P. Fran\c{cois, 2007: Aerosol retrieval over land using a multi-band polarimeter and comparison with path radiance method, *J. Geophys. Res.*, **112**, D111214, doi:10.1029/2006JD008029.

Waquet, F., B. Cairns, K. Knobespiesse, J. Chowdhary, L.D. Travis, B. Schmid, and M.I. Mishchenko, 2009: Polarimetric remote sensing of aerosols over land, *J. Geophys. Res.*, **114**, DOI 1206, doi:1029/2008JD010619.